

# Anisotropic Non-Fermi Liquids

Shouvik Sur<sup>1,\*</sup> and Sung-Sik Lee<sup>1,2</sup>

<sup>1</sup>Department of Physics & Astronomy, McMaster University,  
1280 Main St. W., Hamilton ON L8S 4M1, Canada

<sup>2</sup>Perimeter Institute for Theoretical Physics,  
31 Caroline St. N., Waterloo ON N2L 2Y5, Canada

(Dated: July 28, 2016)

We study non-Fermi liquid states that arise at the quantum critical points associated with the spin density wave (SDW) and charge density wave (CDW) transitions in metals with twofold rotational symmetry. We use the dimensional regularization scheme, where a one-dimensional Fermi surface is embedded in  $3 - \epsilon$  dimensional momentum space. In three dimensions, quasilocal marginal Fermi liquids arise both at the SDW and CDW critical points : the speed of the collective mode along the ordering wavevector is logarithmically renormalized to zero compared to that of Fermi velocity. Below three dimensions, however, the SDW and CDW critical points exhibit drastically different behaviors. At the SDW critical point, a stable anisotropic non-Fermi liquid state is realized for small  $\epsilon$ , where not only time but also different spatial coordinates develop distinct anomalous dimensions. The non-Fermi liquid exhibits an emergent algebraic nesting as the patches of Fermi surface are deformed into a universal power-law shape near the hot spots. Due to the anisotropic scaling, the energy of incoherent spin fluctuations disperse with different power laws in different momentum directions. At the CDW critical point, on the other hand, the perturbative expansion breaks down immediately below three dimensions as the interaction renormalizes the speed of charge fluctuations to zero within a finite renormalization group scale through a two-loop effect. The difference originates from the fact that the vertex correction anti-screens the coupling at the SDW critical point whereas it screens at the CDW critical point.

\* Present address : National High Magnetic Field Laboratory and Department of Physics, Florida State University, Tallahassee, Florida 32306, USA.

## CONTENTS

I. Introduction	1
II. The Model	3
III. Renormalization Group	5
IV. Spin Density Wave Criticality	8
V. Charge Density Wave Criticality	17
VI. Summary and Discussion	19
VII. Acknowledgment	19
References	19
A. Computation of Feynman diagrams	21
B. Analysis of RG flow at the CDW critical point	26

## I. INTRODUCTION

Quantum phase transitions commonly arise in a wide range of strongly correlated metals such as high  $T_c$  cuprates, iron pnictides, and heavy fermion compounds [1–7]. Proximity of metals to symmetry broken phases creates non-Fermi liquid states near quantum critical points through the coupling between soft particle-hole excitations and the order parameter

fluctuations. At the critical point, the low-energy excitations near the Fermi surface strongly damp the order parameter fluctuations which, in turn, feed back to the dynamics of low energy fermions [8–22]. The theoretical challenge is to understand the intricate interplay between the electronic degrees of freedom and the critical fluctuations of order parameter. In two space dimensions, the metallic quantum critical points remain largely ill-understood due to strong coupling between itinerant electrons and the collective modes.

In chiral non-Fermi liquids, strong kinematic constraints protect critical exponents from quantum corrections beyond one-loop, even though it is a strongly coupled theory in two space dimensions [23]. However, such non-perturbative constraints are unavailable for non-chiral systems in general. Therefore, it is of interest to find perturbatively accessible non-Fermi liquids which can be understood in a controlled way. Various deformations of theoretical models have been considered to obtain perturbative control over quantum fluctuations. An introduction of a large number of species of fermions fails to weaken the strong quantum fluctuations in the presence of a Fermi surface [24–27]. To tame quantum fluctuations, one can use a dimensional regularization scheme where the dimension of space is increased with the co-dimension of the Fermi surface fixed to be one [28–30]. This scheme has the merit of preserving a non-vanishing density of states at the Fermi surface. However, the increase in the dimension of Fermi surface beyond one results in a loss of emergent locality in the momentum space [31], which is an example of ultraviolet/infrared (UV/IR) mixing [32]. Consequently, the size of the Fermi surface enters in the low-energy

scaling of physical quantities which are insensitive to the size of Fermi surface in the original two-dimensional theory. An alternative strategy is to reduce the density of states of the collective mode [33, 34], or the fermions [35–37]. This is achieved either by modifying the dispersion, or embedding the one-dimensional Fermi surface in a higher dimensional space. In the latter ‘co-dimensional’ regularization scheme, one can preserve locality and avoid UV/IR mixing by introducing a nodal gap, which leaves behind a one-dimensional Fermi surface embedded in general  $d$  dimensions [36, 37]. Weakly interacting non-Fermi liquids become accessible near the upper critical dimension, where the deviation from the upper critical dimension,  $\epsilon$ , becomes a small parameter.

In a recent work [37], the spin-density wave critical point was studied in metals with four-fold rotational ( $C_4$ ) symmetry based on the co-dimensional regularization scheme. From one-loop renormalization group (RG) analysis, a non-Fermi liquid state was found at the infrared (IR) fixed point below three dimensions. Although interactions are renormalized to zero at low energies, an emergent nesting of Fermi surface and the boson velocity that flows to zero in the low energy limit enhance quantum fluctuations. A balance between the vanishing coupling and the IR singularity caused by the dynamically generated quasilocality results in a stable non-Fermi liquid for small  $\epsilon$ . Here quasilocality is different from a completely dispersionless spectrum of the collective mode [38, 39]. Instead it refers to the fact that the velocity of the collective mode measured in the unit of the Fermi velocity flows to zero in the low energy limit.

The emergent nesting is a consequence of interaction which tends to localize particles in certain directions in real space. However, the effect of the interactions is rather limited in the presence of the  $C_4$  symmetry, which constrains the  $x$  and  $y$  components of momentum to scale identically. Because the deviation from perfect nesting flows to zero only logarithmically in length scale [20, 21, 26, 37, 39], the Fermi surface nesting becomes noticeable only when the momentum is exponentially close to the hot spots. The situation is different when the  $C_4$  symmetry is explicitly or spontaneously broken to two-fold rotational ( $C_2$ ) symmetry [40–48]. If the system undergoes a continuous density wave transition in metals with the  $C_2$  symmetry [49–53], a new type of non-Fermi can emerge at the quantum critical point. Because different components of momentum receive different quantum corrections, the system can exhibit a stronger dynamical nesting. In this paper, we study the scaling properties of the quantum critical points associated with the spin density wave (SDW) and charge density wave (CDW) transitions in metals with the  $C_2$  symmetry (see Fig. 1).

The paper is organized as follows. In section II, we introduce the low energy effective theory that describes the density wave critical points in metals with the  $C_2$  symmetry. We take advantage of the formal similarities between the SDW and CDW critical points to formulate a unified approach to both cases. Here we employ the co-dimensional regularization scheme, where the one-dimensional Fermi surface is embedded in  $3 - \epsilon$  space dimensions. In section III, we outline the RG procedure, and derive the general expressions for the

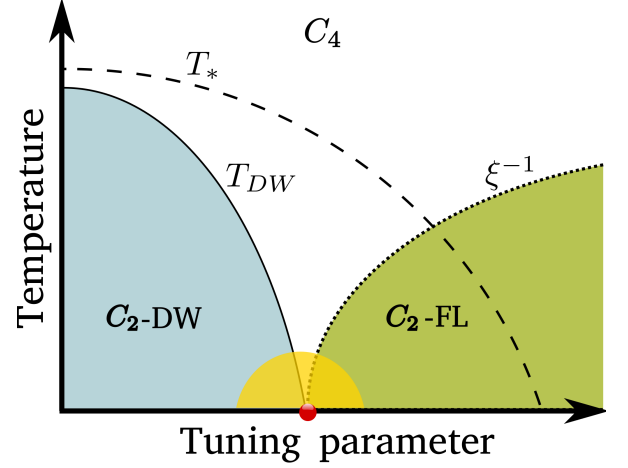


FIG. 1: A schematic phase diagram for a density wave transition in metals with the  $C_2$  symmetry. Here ‘DW’ = density wave, and ‘FL’ = Fermi liquid.  $T_*$  (dashed line) is a temperature scale which separates the  $C_2$  symmetric phase at low temperatures from the  $C_4$  symmetric phase at high temperatures.  $T_*$  is a crossover when  $C_4$  is explicitly broken, whereas it becomes a phase transition line when  $C_4$  is spontaneously broken. Either way, the quantum critical point for the density wave transition is described by the same theory that respects only  $C_2$  symmetry.  $T_{DW}$  (solid line) is the temperature scale below which the system develops a long-range density wave order.  $\xi^{-1}$  (dotted line) is the inverse correlation length of the density wave fluctuations in the paramagnetic Fermi liquid. The dome around the critical point represents a potential secondary ordered phase that can appear if the critical point is unstable.

critical exponents and the beta functions. In section IV, we show that a stable non-Fermi liquid fixed point is realized at the SDW critical point slightly below three dimensions. In the low energy limit, not only frequency but also different momentum components acquire anomalous dimensions, resulting in an anisotropic non-Fermi liquid. We compute the critical exponents that govern the anisotropy, and other critical exponents to the leading order in  $\epsilon$ . In the low energy limit, the energy of the collective mode disperses with different powers in different momentum directions. Furthermore, the Fermi surface near the hot spots connected by the SDW vector is deformed to a universal power-law shape. The algebraic nesting is stronger compared to the  $C_4$  symmetric case where the Fermi surface is deformed only logarithmically. It is also shown that a component of the boson velocity, which flows to zero at the one-loop order, flows to a nonzero value which is order of  $\epsilon^{1/3}$  due to a two-loop correction. The non-zero but small velocity enhances higher-loop diagrams. Despite the enhancement, higher loop corrections are systematically suppressed in the small  $\epsilon$  limit, and the  $\epsilon$ -expansion is controlled. Section V is devoted to the CDW critical point. Although the system flows to a stable marginal Fermi liquid in three dimensions, it flows out of the perturbative window in the low energy limit for any nonzero  $\epsilon$ . In section VI, we

conclude with a summary.

## II. THE MODEL

In this section we introduce the minimal model for the quantum critical point associated with the spin and charge density wave transitions in metals with the  $C_2$  symmetry. A rectangular lattice with anisotropic hoppings in the  $\hat{x}$  and  $\hat{y}$  directions gives an anisotropic Fermi surface as is shown in Fig. 2a. At a generic filling, the Fermi surface is not nested, and weak interactions do not produce density wave instabilities. Here we assume that there exists a microscopic Hamiltonian with a finite strength of interaction that drives a spin or charge density wave transition in the  $C_2$  symmetric metal. We consider a commensurate density wave with wave vector  $\vec{Q}_{ord}$  which satisfies  $2\vec{Q}_{ord} = 0$  modulo the reciprocal vectors. The specific choice of  $\vec{Q}_{ord}$  and the shape of the Fermi surface is unimportant for the low energy description of the quantum critical point. The order parameter fluctuations are

strongly coupled with electrons near a finite number of hot spots which are connected to each other through the primary wave vector  $\vec{Q}_{ord}$ . The hot spots are represented as (red) dots in Fig. 2b. In the ordered state, the Fermi surface is reconstructed (see Fig. 2c) due to a gap that opens up in the single particle excitation spectrum near the hot spots.

We study the universal properties of the critical points within the framework of low energy effective field theory that is independent of the microscopic details. A spin-fermion model is the minimal theory that describes the interaction between the collective mode and the itinerant electrons [20, 21]. In the minimal model, we focus on the vicinity of the hot spots and consider interactions of the electrons near the hot spots with long wavelength fluctuations of the order parameter. At low energies, we can ignore the Fermi surface curvature and use linearized electronic dispersions around the hot spots. We emphasize that linearizing the dispersion is not equivalent to taking the one-dimensional limit because the collective modes scatter electrons across the hot spots whose Fermi velocities are not parallel to each other. Due to the similarities between the SDW and CDW critical points, we introduce a general action which is applicable to both cases,

$$\begin{aligned}
S = & \sum_{j=1}^{N_f} \sum_{s=1}^{N_c} \sum_{l=1}^2 \sum_{m=\pm} \int \frac{d^3k}{(2\pi)^3} \psi_{l,m,j,s}^*(k) \left( ik_0 + \vec{v}_{l,m} \cdot \vec{k} \right) \psi_{l,m,j,s}(k) + \frac{1}{4} \int \frac{d^3q}{(2\pi)^3} (q_0^2 + c_x^2 q_x^2 + c_y^2 q_y^2) \text{Tr}(\Phi(-q)\Phi(q)) \\
& + \frac{\tilde{g}}{\sqrt{N_f}} \sum_{j=1}^{N_f} \sum_{l=1}^2 \sum_{s,s'=1}^{N_c} \int \frac{d^3k}{(2\pi)^3} \frac{d^3q}{(2\pi)^3} [\psi_{l,+,j,s}^*(k+q) \Phi_{s,s'}(q) \psi_{l,-,j,s'}(k) + \text{h.c.}] \\
& + \frac{1}{4} \int \frac{d^3q_1}{(2\pi)^3} \frac{d^3q_2}{(2\pi)^3} \frac{d^3q_3}{(2\pi)^3} \left[ \tilde{u}_1 \text{Tr}(\Phi(-q_1+q_2)\Phi(q_1)) \text{Tr}(\Phi(-q_3-q_2)\Phi(q_3)) \right. \\
& \left. + \tilde{u}_2 \text{Tr}(\Phi(-q_1+q_2)\Phi(q_1)\Phi(-q_3-q_2)\Phi(q_3)) \right]. \tag{1}
\end{aligned}$$

Here  $\psi_{l,m,j,s}(k)$  describe electrons with momenta near the hot spots, where  $(l,m)$  with  $l = 1, 2$  and  $m = \pm$  labels the four hot spots as shown in Fig. 2b.  $j = 1, 2, \dots, N_f$  and  $s = 1, 2, \dots, N_c$  represent a flavor index and the spin, respectively. The  $SU(2)$  spin is generalized to  $SU(N_c)$ . The parameter  $N_f$  is an extra flavor which can arise from degenerate bands with the  $SU(N_f)$  symmetry.  $\vec{k}$  is the two-dimensional momentum that measures a deviation from the hot spots.  $\vec{v}_{l,m}$  is the Fermi velocity at each hot spot:  $\vec{v}_{1,+} \equiv (v_x, v_y) = -\vec{v}_{2,+}$ ,  $\vec{v}_{1,-} \equiv (v_x, -v_y) = -\vec{v}_{2,-}$ . If the ordering wave vector happens to coincide with  $2\vec{K}_F$  ( $\vec{K}_F$  being a Fermi vector),  $v_x$  vanishes and one needs to include the local curvature of the Fermi surface[54, 55]. In this paper, we consider the generic case with  $v_x, v_y > 0$ , where the hot spots connected by the order vector are not pre-nested. The  $N_c \times N_c$  matrix field  $\Phi(q)$  represents the density wave mode of frequency  $q_0$  and momentum  $\vec{Q}_{ord} + \vec{q}$ . The boson field satisfies  $\Phi^\dagger(q) = \Phi(-q)$

because  $2\vec{Q}_{ord} = 0$  [56]. The matrix field can be written as

$$\Phi(q) = \begin{cases} \vec{\phi}(q) \cdot \vec{\tau} & \text{for SDW} \\ \sqrt{\frac{2}{N_c}} \phi(q) \mathcal{I}_{N_c} & \text{for CDW} \end{cases} \tag{2}$$

where  $\tau^{(\alpha)}$  is the  $\alpha$ -th generator of  $SU(N_c)$  in the fundamental representation, and  $\mathcal{I}_{N_c}$  is the  $N_c \times N_c$  identity matrix.  $\tau^{(\alpha)}$  and  $\mathcal{I}_{N_c}$  represent the spin and charge vertices, respectively. We choose the normalization  $\text{Tr}(\tau^{(\alpha)}\tau^{(\beta)}) = 2\delta^{\alpha\beta}$  for the  $\tau$ -matrices. For  $N_c = 2$  and 3 in the SDW case and for any  $N_c$  in the CDW case,  $\tilde{u}_1$  and  $\tilde{u}_2$  are equivalent, and we can set  $\tilde{u}_2 = 0$  without loss of generality. For the CDW critical point, both  $N_f$  and  $N_c$  play the same role, and the physics depends only on the total number of electron species,  $\tilde{N}_f = N_c N_f$ .

Some parameters in Eq. (1) can be absorbed into scales of momentum and fields. We scale  $(k_x, k_y) \mapsto \left(\frac{k_x}{c_x}, \frac{k_y}{c_y}\right)$  and  $(\Phi, \psi) \mapsto \sqrt{c_x c_y}(\Phi, \psi)$  to rewrite the action as

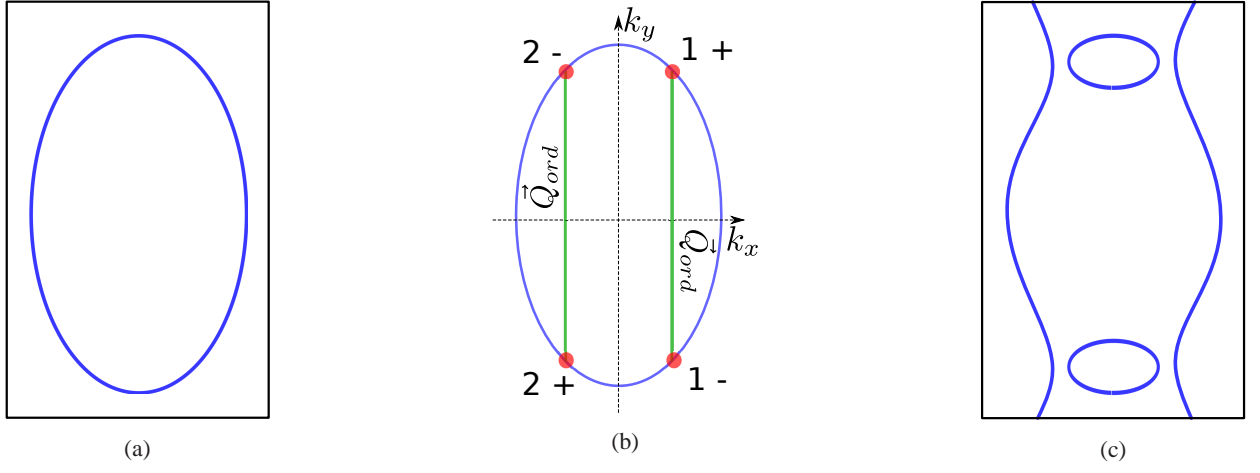


FIG. 2: (a) Anisotropic Fermi surface in two space dimensions. (b) At the critical point, density wave fluctuations induce strong scatterings between electrons near the hot spots denoted by the red dots. (c) Reconstructed Fermi surface in the ordered phase.

$$\begin{aligned}
S = & \sum_{j=1}^{N_f} \sum_{s=1}^{N_c} \sum_{l=1}^2 \sum_{m=\pm} \int \frac{d^3 k}{(2\pi)^3} \psi_{l,m,j,s}^*(k) \left( i k_0 + \mathcal{E}_{l,m}(\vec{k}) \right) \psi_{l,m,j,s}(k) + \frac{1}{4} \int \frac{d^3 q}{(2\pi)^3} (q_0^2 + q_x^2 + c^2 q_y^2) \text{Tr}(\Phi(-q)\Phi(q)) \\
& + \frac{g_0}{\sqrt{N_f}} \sum_{j=1}^{N_f} \sum_{l=1}^2 \sum_{s,s'=1}^{N_c} \int \frac{d^3 k}{(2\pi)^3} \frac{d^3 q}{(2\pi)^3} [\psi_{l,+,j,s}^*(k+q) \Phi_{s,s'}(q) \psi_{l,-,j,s'}(k) + \text{h.c.}] \\
& + \frac{1}{4} \int \frac{d^3 q_1}{(2\pi)^3} \frac{d^3 q_2}{(2\pi)^3} \frac{d^3 q_3}{(2\pi)^3} \left[ u_{1;0} \text{Tr}(\Phi(-q_1 + q_2)\Phi(q_1)) \text{Tr}(\Phi(-q_3 - q_2)\Phi(q_3)) \right. \\
& \left. + u_{2;0} \text{Tr}(\Phi(-q_1 + q_2)\Phi(q_1)\Phi(-q_3 - q_2)\Phi(q_3)) \right]. \tag{3}
\end{aligned}$$

The rescaled dispersions are  $\mathcal{E}_{1,+}(\vec{k}) = -\mathcal{E}_{2,+}(\vec{k}) = vk_x + k_y$ , and  $\mathcal{E}_{1,-}(\vec{k}) = -\mathcal{E}_{2,-}(\vec{k}) = vk_x - k_y$ , where  $v \equiv \frac{v_x}{c_x}$  and  $c \equiv \frac{c_y}{v_y}$  represent the relative velocities between electron and boson in the two directions. The couplings are also rescaled to  $g_0 \equiv \frac{\tilde{g}}{\sqrt{c_x v_y}}$  and  $u_{i;0} \equiv \frac{\tilde{u}_i}{c_x v_y}$ .

The  $(2 + 1)$ -dimensional theory is now generalized to

a  $(d + 1)$ -dimensional theory which describes the one-dimensional Fermi surface embedded in  $d$ -dimensional momentum space. Following the formalism in Ref. [37], we express Eq. (3) in the basis of spinors  $\Psi_{+,j,s}(k) = (\psi_{1,+,j,s}(k), \psi_{2,+,j,s}(k))^T$  and  $\Psi_{-,j;s}(k) = (\psi_{1,-,j;s}(k), -\psi_{2,-,j;s}(k))^T$ , and add  $(d - 2)$  extra co-dimensions to the Fermi surface,

$$\begin{aligned}
S = & \sum_{j=1}^{N_f} \sum_{s=1}^{N_c} \sum_{n=\pm} \int dk \bar{\Psi}_{n,j,s}(k) \left( i \mathbf{K} \cdot \mathbf{\Gamma} + i \varepsilon_n(\vec{k}) \gamma_{d-1} \right) \Psi_{n,j,s}(k) + \frac{1}{4} \int dq (|\mathbf{Q}|^2 + q_x^2 + c^2 q_y^2) \text{Tr}(\Phi(-q)\Phi(q)) \\
& + i \frac{g_0}{\sqrt{N_f}} \sum_{j=1}^{N_f} \sum_{s,s'=1}^{N_c} \int dk dq [\bar{\Psi}_{+,j,s}(k+q) \gamma_{d-1} \Phi_{s,s'}(q) \Psi_{-,j;s'}(k) - \text{h.c.}] \\
& + \frac{1}{4} \int dq_1 dq_2 dq_3 \left[ u_{1;0} \text{Tr}(\Phi(-q_1 + q_2)\Phi(q_1)) \text{Tr}(\Phi(-q_3 - q_2)\Phi(q_3)) + u_{2;0} \text{Tr}(\Phi(-q_1 + q_2)\Phi(q_1)\Phi(-q_3 - q_2)\Phi(q_3)) \right], \tag{4}
\end{aligned}$$

where  $k \equiv (\mathbf{K}, \vec{k})$  and  $dk \equiv \frac{d^{d+1}k}{(2\pi)^{d+1}}$ . The two dimensional vectors on the plane of the Fermi surface are denoted as  $\vec{k} = (k_x, k_y)$ , while  $\mathbf{K} = (k_0, k_1, \dots, k_{d-2})$  denotes  $(d-1)$  dimensional vectors with  $k_1, \dots, k_{d-2}$  being the newly added co-dimensions. We collect the first  $(d-1)$   $\gamma$ -matrices in  $\mathbf{\Gamma} = (\gamma_0, \gamma_1, \dots, \gamma_{d-2})$ . The conjugate spinor is defined by  $\bar{\Psi}_{n,j,s} = \Psi_{n,j,s}^\dagger \gamma_0$ . The dispersions of the spinors along the  $\vec{k}$  direction are inherited from the two dimensional dispersion,  $\varepsilon_\pm(\vec{k}) = vk_x \pm k_y$ . It is easy to check that we recover Eq. (3) in  $d = 2$  with  $\gamma_0 = \sigma_y$  and  $\gamma_1 = \sigma_x$ , where  $\sigma_i$  are Pauli matrices. The theory in general dimensions interpolate between the two-dimensional metal and a semi-metal with a line node in three dimensions [57, 58]. The action is invariant under  $U(1) \times SU(N_c) \times SU(N_f)$ , which are associated with the particle number, spin and flavor conservations, respectively. The theory is also invariant under time reversal, inversion, and  $SO(d-1)$  rotations in  $\mathbf{K}$ .

The engineering scaling dimensions of the  $(d+1)$ -momentum, the fields and the couplings are

$$[\mathbf{K}] = 1, \quad [k_x] = 1, \quad [k_y] = 1, \\ [\Psi_{n,j,s}] = -\frac{1}{2}(d+2), \quad [\Phi] = -\frac{1}{2}(d+3), \quad [v] = 0$$

$$[c] = 0, \quad [g_0] = \frac{1}{2}(3-d), \quad \text{and} \quad [u_0] = 3-d. \quad (5)$$

Classically, frequency and all momentum components have the same scaling dimension. The upper critical dimension is  $d = 3$  at which all the couplings in the theory are dimensionless at the Gaussian fixed point. We apply the field theoretic RG based on a perturbative expansion in  $\epsilon \equiv 3-d$ .

### III. RENORMALIZATION GROUP

In this section we outline our RG scheme, and derive the general expressions for the beta functions and the critical exponents. The readers who wish to skip the details can jump to Eqs. (17) - (27) which are the main results of this section.

Starting with the action in Eq. (4), we define dimensionless couplings

$$g = \mu^{-(3-d)/2} g_0, \quad u_i = \mu^{-(3-d)} u_{i;0}, \quad (6)$$

where  $\mu$  is a scale at which the renormalized couplings are to be defined. From the action in Eq. (4), the quantum effective action is computed perturbatively in the couplings. The logarithmic divergences that arise at the upper critical dimension manifest themselves as poles in  $\epsilon$ . Requiring the renormalized quantum effective action to be analytic in  $\epsilon$ , we add counter terms of the form,

$$S_{CT} = \sum_{j=1}^{N_f} \sum_{s=1}^{N_c} \sum_{n=\pm} \int dk \bar{\Psi}_{n,j,s}(k) (i\mathcal{A}_1 \mathbf{K} \cdot \mathbf{\Gamma} + i(\mathcal{A}_2 vk_x + n\mathcal{A}_3 k_y) \gamma_{d-1}) \Psi_{n,j,s}(k) \\ + \frac{1}{4} \int dq (\mathcal{A}_4 |\mathbf{Q}|^2 + \mathcal{A}_5 q_x^2 + \mathcal{A}_6 c^2 q_y^2) \text{Tr}(\Phi(-q)\Phi(q)) \\ + \mathcal{A}_7 \mu^{(3-d)/2} \frac{ig}{\sqrt{N_f}} \sum_{j=1}^{N_f} \sum_{s,s'=1}^{N_c} \int dk dq [\bar{\Psi}_{+,j,s}(k+q) \gamma_{d-1} \Phi_{s,s'}(q) \Psi_{-,j,s'}(k) - \text{h.c.}] \\ + \frac{\mu^{(3-d)}}{4} \int dq_1 dq_2 dq_3 [\mathcal{A}_8 u_1 \text{Tr}(\Phi(-q_1+q_2)\Phi(q_1)) \text{Tr}(\Phi(-q_3-q_2)\Phi(q_3)) \\ + \mathcal{A}_9 u_2 \text{Tr}(\Phi(-q_1+q_2)\Phi(q_1)\Phi(-q_3-q_2)\Phi(q_3))], \quad (7)$$

with  $\mathcal{A}_i \equiv \mathcal{A}_i(v, c, g, u, \epsilon) = \sum_{m=1}^{\infty} Z_{i,m}(v, c, g, u) \epsilon^{-m}$ . The counter terms are chosen to cancel the poles in  $\epsilon$  based on the minimal subtraction scheme. Due to the lack of full rotational symmetry in the  $(\mathbf{K}, \vec{k})$ -space and the  $C_4$  symmetry in the  $(k_x, k_y)$ -plane, the kinetic terms are renormalized differ-

ently in the  $\mathbf{K}$ ,  $k_x$ , and  $k_y$  directions, respectively. Therefore,  $\mathbf{K}$ ,  $k_x$  and  $k_y$  can have different quantum scaling dimensions. The sum of the original action and the counter terms gives the bare action,

$$S_B = \sum_{j=1}^{N_f} \sum_{s=1}^{N_c} \sum_{n=\pm} \int dk_B \bar{\Psi}_{B;n,j,s}(k_B) (i\mathbf{K}_B \cdot \mathbf{\Gamma} + i(v_B k_{B;x} + n k_{B;y}) \gamma_{d-1}) \Psi_{B;n,j,s}(k_B)$$



$$\begin{aligned}
& + \frac{1}{4} \int dq_B (|\mathbf{Q}_B|^2 + q_{B;x}^2 + c_B^2 q_{B;y}^2) \text{Tr}(\Phi_B(-q_B)\Phi_B(q_B)) \\
& + i \frac{g_B}{\sqrt{N_f}} \sum_{j=1}^{N_f} \sum_{s,s'=1}^{N_c} \int dk_B dq_B [\bar{\Psi}_{B;+,j,s}(k_B + q_B) \gamma_{d-1} \Phi_{B;s,s'}(q_B) \Psi_{B;- ,j,s'}(k_B) - \text{h.c.}] \\
& + \frac{1}{4} \int dq_{1;B} dq_{2;B} dq_{3;B} \left[ u_{1;B} \text{Tr}(\Phi_B(-q_{1;B} + q_{2;B})\Phi_B(q_{1;B})) \text{Tr}(\Phi_B(-q_{3;B} - q_{2;B})\Phi_B(q_{3;B})) \right. \\
& \quad \left. + u_{2;B} \text{Tr}(\Phi_B(-q_{1;B} + q_{2;B})\Phi_B(q_{1;B})\Phi_B(-q_{3;B} - q_{2;B})\Phi_B(q_{3;B})) \right]. \quad (8)
\end{aligned}$$

Here the bare quantities are related to their renormalized counterparts through the multiplicative factors,

$$\begin{aligned}
\mathbf{K} &= \mathcal{Z}_\tau^{-1} \mathbf{K}_B, & k_x &= \mathcal{Z}_x^{-1} k_{B;x}, \\
k_y &= k_{B;y}, & \Psi_{n,j,s} &= \mathcal{Z}_\psi^{-\frac{1}{2}} \Psi_{B;n,j,s}, \\
\Phi &= \mathcal{Z}_\phi^{-\frac{1}{2}} \Phi_B, & v &= \frac{\mathcal{Z}_x^2 \mathcal{Z}_\tau^{d-1} \mathcal{Z}_\psi}{\mathcal{Z}_2} v_B, \\
c &= \left[ \frac{\mathcal{Z}_x \mathcal{Z}_\phi \mathcal{Z}_\tau^{d-1}}{\mathcal{Z}_6} \right]^{\frac{1}{2}} c_B, \\
g &= \mu^{-(3-d)/2} \frac{\mathcal{Z}_x^2 \mathcal{Z}_\tau^{2(d-1)} \mathcal{Z}_\psi \mathcal{Z}_\phi^{\frac{1}{2}}}{\mathcal{Z}_7} g_B, \\
u_1 &= \mu^{-(3-d)} \frac{\mathcal{Z}_x^3 \mathcal{Z}_\tau^{3(d-1)} \mathcal{Z}_\phi^2}{\mathcal{Z}_8} u_{1;B}, \\
u_2 &= \mu^{-(3-d)} \frac{\mathcal{Z}_x^3 \mathcal{Z}_\tau^{3(d-1)} \mathcal{Z}_\phi^2}{\mathcal{Z}_9} u_{2;B}, \quad (9)
\end{aligned}$$

where

$$\mathcal{Z}_\tau = \frac{\mathcal{Z}_1}{\mathcal{Z}_3}, \quad \mathcal{Z}_x = \mathcal{Z}_\tau \left[ \frac{\mathcal{Z}_5}{\mathcal{Z}_4} \right]^{1/2},$$

$$\mathcal{Z}_\psi = \frac{\mathcal{Z}_3}{\mathcal{Z}_x \mathcal{Z}_\tau^{(d-1)}}, \quad \mathcal{Z}_\phi = \frac{\mathcal{Z}_4}{\mathcal{Z}_x \mathcal{Z}_\tau^{(d+1)}}, \quad (10)$$

with  $\mathcal{Z}_i \equiv 1 + \mathcal{A}_i(v, c, g, u, \epsilon)$ . Here we made the choice  $k_y = k_{B;y}$ , which fixes the scaling dimension of  $k_y$  to be 1. This choice can be always made, even at the quantum level, because one can measure scaling dimensions of other quantities with respect to that of  $k_y$ .  $\mathcal{Z}_\tau$  and  $\mathcal{Z}_x$  encode the anisotropic quantum corrections, which lead to anomalous dimensions for  $\mathbf{K}$  and  $k_x$ .

The renormalization group equation is obtained by requiring that the bare Green's function is invariant under the change of the scale  $\mu$  at which the renormalized vertex functions are defined. The renormalized Green's function,

$$\begin{aligned}
& \langle \Phi(q_1) \dots \Phi(q_b) \Psi(k_1) \dots \Psi(k_f) \bar{\Psi}(k_{f+1}) \dots \bar{\Psi}(k_{2f}) \rangle \\
& \equiv G^{(2f,b)}(q_i, k_j; v, c, g, u; \mu) \\
& \times \delta^{(d+1)} \left( \sum_{i=1}^b q_i + \sum_{j=1}^f (k_j - k_{f+j}) \right), \quad (11)
\end{aligned}$$

obeys the renormalization group equation,

$$\begin{aligned}
& \left[ z_\tau (\mathbf{K}_j \cdot \nabla_{\mathbf{K}_j} + \mathbf{Q}_i \cdot \nabla_{\mathbf{Q}_i}) + z_x (k_{j;x} \partial_{k_{j;x}} + q_{i;x} \partial_{q_{i;x}}) + (k_{j;y} \partial_{k_{j;y}} + q_{i;y} \partial_{q_{i;y}}) \right. \\
& - \beta_v \frac{\partial}{\partial v} - \beta_c \frac{\partial}{\partial c} - \beta_g \frac{\partial}{\partial g} - \beta_{u_1} \frac{\partial}{\partial u_1} - \beta_{u_2} \frac{\partial}{\partial u_2} \\
& \left. + 2f \left( \frac{d+2}{2} - \eta_\psi \right) + b \left( \frac{d+3}{2} - \eta_\phi \right) - (z_\tau (d-1) + z_x + 1) \right] G^{(2f,b)}(q_i, k_j; v, c, g, u; \mu) = 0. \quad (12)
\end{aligned}$$

Here  $z_\tau$  and  $z_x$  are the quantum scaling dimensions for  $\mathbf{K}$  and  $k_x$  given by

$$z_\tau = 1 + \frac{\partial \ln \mathcal{Z}_\tau}{\partial \ln \mu}, \quad z_x = 1 + \frac{\partial \ln \mathcal{Z}_x}{\partial \ln \mu}, \quad (13)$$

and  $\eta_\psi$  and  $\eta_\phi$  are the anomalous dimensions of the fields,

$$\eta_\psi = \frac{1}{2} \frac{\partial \ln \mathcal{Z}_\psi}{\partial \ln \mu}, \quad \eta_\phi = \frac{1}{2} \frac{\partial \ln \mathcal{Z}_\phi}{\partial \ln \mu}. \quad (14)$$

The beta functions, which describe the change of couplings

with an increasing energy scale, are defined as

$$\begin{aligned}\beta_v &= \frac{\partial v}{\partial \ln \mu}, & \beta_c &= \frac{\partial c}{\partial \ln \mu}, \\ \beta_g &= \frac{\partial g}{\partial \ln \mu}, & \beta_{u_i} &= \frac{\partial u_i}{\partial \ln \mu}.\end{aligned}\quad (15)$$

We use the relationship between the bare and renormalized quantities defined in Eq. (9) to obtain a set of coupled differential equations,

$$\begin{aligned}\mathcal{Z}_1 \left[ d(z_\tau - 1) + (z_x - 1) + 2\eta_\psi \right] - \frac{\partial \mathcal{Z}_1}{\partial \ln \mu} &= 0, \\ \mathcal{Z}_2 \left[ \beta_v - v \{ (d-1)(z_\tau - 1) + 2(z_x - 1) + 2\eta_\psi \} \right] \\ &\quad + v \frac{\partial \mathcal{Z}_2}{\partial \ln \mu} = 0, \\ \mathcal{Z}_3 \left[ (d-1)(z_\tau - 1) + (z_x - 1) + 2\eta_\psi \right] - \frac{\partial \mathcal{Z}_3}{\partial \ln \mu} &= 0, \\ \mathcal{Z}_4 \left[ (d+1)(z_\tau - 1) + (z_x - 1) + 2\eta_\phi \right] - \frac{\partial \mathcal{Z}_4}{\partial \ln \mu} &= 0, \\ \mathcal{Z}_5 \left[ (d-1)(z_\tau - 1) + 3(z_x - 1) + 2\eta_\phi \right] - \frac{\partial \mathcal{Z}_5}{\partial \ln \mu} &= 0,\end{aligned}$$

$$\begin{aligned}\mathcal{Z}_6 \left[ 2\beta_c - c \{ (d-1)(z_\tau - 1) + (z_x - 1) + 2\eta_\phi \} \right] \\ &\quad + c \frac{\partial \mathcal{Z}_6}{\partial \ln \mu} = 0, \\ \mathcal{Z}_7 \left[ \beta_g - g \left\{ -\frac{3-d}{2} + 2(d-1)(z_\tau - 1) + 2(z_x - 1) \right. \right. \\ &\quad \left. \left. + 2\eta_\psi + \eta_\phi \right\} \right] + g \frac{\partial \mathcal{Z}_7}{\partial \ln \mu} = 0, \\ \mathcal{Z}_8 \left[ \beta_{u_1} - u_1 \left\{ -(3-d) + 3(d-1)(z_\tau - 1) + 3(z_x - 1) \right. \right. \\ &\quad \left. \left. + 4\eta_\phi \right\} \right] + u_1 \frac{\partial \mathcal{Z}_8}{\partial \ln \mu} = 0, \\ \mathcal{Z}_9 \left[ \beta_{u_2} - u_2 \left\{ -(3-d) + 3(d-1)(z_\tau - 1) + 3(z_x - 1) \right. \right. \\ &\quad \left. \left. + 4\eta_\phi \right\} \right] + u_2 \frac{\partial \mathcal{Z}_9}{\partial \ln \mu} = 0,\end{aligned}\quad (16)$$

which are solved to obtain the expressions for the critical exponents and the beta functions,

$$z_\tau = \left[ 1 + \left( \frac{1}{2} g \partial_g + \sum_i u_i \partial_{u_i} \right) (Z_{1,1} - Z_{3,1}) \right]^{-1}, \quad (17)$$

$$z_x = 1 - \frac{1}{2} z_\tau \left( \frac{1}{2} g \partial_g + \sum_i u_i \partial_{u_i} \right) (2Z_{1,1} - 2Z_{3,1} - Z_{4,1} + Z_{5,1}), \quad (18)$$

$$\eta_\psi = \frac{\epsilon}{2} (z_\tau - 1) - \frac{1}{2} \left[ 2(z_\tau - 1) + (z_x - 1) + z_\tau \left( \frac{1}{2} g \partial_g + \sum_i u_i \partial_{u_i} \right) Z_{3,1} \right], \quad (19)$$

$$\eta_\phi = \frac{\epsilon}{2} (z_\tau - 1) - \frac{1}{2} \left[ 4(z_\tau - 1) + (z_x - 1) + z_\tau \left( \frac{1}{2} g \partial_g + \sum_i u_i \partial_{u_i} \right) Z_{4,1} \right], \quad (20)$$

$$\partial_\ell v = \frac{1}{2} z_\tau v \left( \frac{1}{2} g \partial_g + \sum_i u_i \partial_{u_i} \right) (2Z_{1,1} - 2Z_{2,1} - Z_{4,1} + Z_{5,1}), \quad (21)$$

$$\partial_\ell c = -\frac{1}{2} z_\tau c \left( \frac{1}{2} g \partial_g + \sum_i u_i \partial_{u_i} \right) (2Z_{1,1} - 2Z_{3,1} - Z_{4,1} + Z_{6,1}), \quad (22)$$

$$\partial_\ell g = \frac{1}{4} z_\tau g \left[ 2\epsilon + \left( \frac{1}{2} g \partial_g + \sum_i u_i \partial_{u_i} \right) (2Z_{1,1} + 2Z_{3,1} + Z_{4,1} + Z_{5,1} - 4Z_{7,1}) \right], \quad (23)$$

$$\partial_\ell u_1 = \frac{1}{2} z_\tau u_1 \left[ 2\epsilon - \left( \frac{1}{2} g \partial_g + \sum_i u_i \partial_{u_i} \right) (2Z_{1,1} - 2Z_{3,1} - 3Z_{4,1} - Z_{5,1} + 2Z_{8,1}) \right], \quad (24)$$

$$\partial_\ell u_2 = \frac{1}{2} z_\tau u_2 \left[ 2\epsilon - \left( \frac{1}{2} g \partial_g + \sum_i u_i \partial_{u_i} \right) (2Z_{1,1} - 2Z_{3,1} - 3Z_{4,1} - Z_{5,1} + 2Z_{9,1}) \right], \quad (25)$$

where we introduced the IR beta function,  $\partial_\ell \lambda = -\beta_\lambda$  which describes the RG flow with an increase of the logarithmic

length scale  $\ell$ .

In the absence of the Yukawa coupling, every quartic cou-

pling  $u_i$  is accompanied by  $1/c$  in the perturbative series. This reflects the IR singularity for the flat bosonic band in the  $c \rightarrow 0$  limit. Since the actual perturbative expansion is orga-

nized in terms of  $u_i/c$ , it is convenient to introduce  $\chi_i = u_i/c$ . The beta functions for  $\chi_i$  can be readily obtained from those of  $u_i$  and  $c$ ,

$$\partial_\ell \chi_1 = \frac{1}{2} z_\tau \chi_1 \left[ 2\epsilon + \left( \frac{1}{2} g \partial_g + \sum_i u_i \partial_{u_i} \right) (2Z_{4,1} + Z_{5,1} + Z_{6,1} - 2Z_{8,1}) \right], \quad (26)$$

$$\partial_\ell \chi_2 = \frac{1}{2} z_\tau \chi_2 \left[ 2\epsilon + \left( \frac{1}{2} g \partial_g + \sum_i u_i \partial_{u_i} \right) (2Z_{4,1} + Z_{5,1} + Z_{6,1} - 2Z_{9,1}) \right]. \quad (27)$$

#### IV. SPIN DENSITY WAVE CRITICALITY

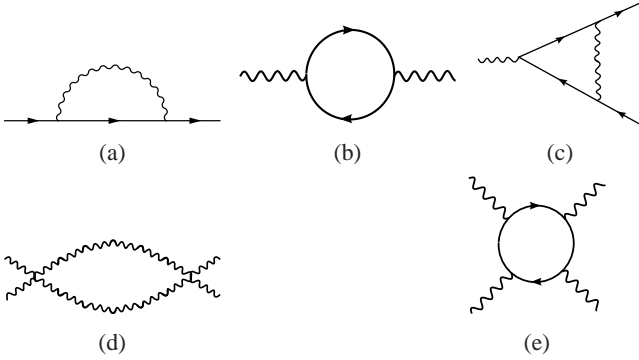


FIG. 3: The one-loop Feynman diagrams. The solid (wiggly) line represents the electron (boson) propagator.

We have introduced the minimal theories for the SDW and CDW critical points. Despite the similarities between the two theories, the behaviors of the two are quite different. The difference originates from the non-abelian and abelian nature of the Yukawa vertex in Eq. (2) for the SDW and CDW theories, respectively. In this section, we will focus on the SDW case, and return to the CDW case in section V.

##### A. One Loop

In this subsection we present the one-loop analysis for the SDW critical point. From the one-loop diagrams shown in Fig. 3, we obtain the following counter terms (see Appendix A for details of the calculation),

$$Z_{1,1} = -\frac{(N_c^2 - 1)}{4\pi^2 N_c N_f} g^2 h_1(v, c),$$

$$Z_{2,1} = \frac{(N_c^2 - 1)}{4\pi^2 N_c N_f} g^2 h_2(v, c)$$

$$\begin{aligned} Z_{3,1} &= -\frac{(N_c^2 - 1)}{4\pi^2 N_c N_f} g^2 h_2(v, c) \\ Z_{4,1} &= -\frac{1}{8\pi} \frac{g^2}{v}, \\ Z_{5,1}, Z_{6,1} &= 0, \\ Z_{7,1} &= -\frac{1}{8\pi^3 N_c N_f} g^2 v h_3(v, c), \\ Z_{8,1} &= \frac{N_c^2 + 7}{2\pi^2} \chi_1 + \frac{2N_c^2 - 3}{\pi^2 N_c} \chi_2 + \frac{3(N_c^2 + 3)}{2\pi^2 N_c^2} \chi_2^2, \\ Z_{9,1} &= \frac{6}{\pi^2} \chi_1 + \frac{2(N_c^2 - 9)}{2\pi^2 N_c} \chi_2, \end{aligned} \quad (28)$$

where

$$\begin{aligned} h_1(v, c) &= \int_0^1 dx \sqrt{\frac{1-x}{c^2 + x(1-(1-v^2)c^2)}}, \\ h_2(v, c) &= c^2 \int_0^1 dx \sqrt{\frac{1-x}{[c^2 + x(1-(1-v^2)c^2)]^3}}, \\ h_3(v, c) &= \int_0^{2\pi} d\theta \int_0^1 dx_1 \int_0^{1-x_1} dx_2 \left[ \frac{1}{\zeta(\theta, x_1, x_2, v, c)} \right. \\ &\quad \left. - \frac{v^2 \sin(2\theta)}{\zeta^2(\theta, x_1, x_2, v, c)} \right] \end{aligned} \quad (29)$$

with

$$\begin{aligned} \zeta(\theta, x_1, x_2, v, c) &= 2v^2 [x_1 \sin^2(\theta) + x_2 \cos^2(\theta)] \\ &\quad + (1 - x_1 - x_2) \left[ \sin^2 \left( \theta + \frac{\pi}{4} \right) + c^2 v^2 \cos^2 \left( \theta + \frac{\pi}{4} \right) \right]. \end{aligned} \quad (30)$$

From Eqs. (17) - (27), and Eq. (28), we obtain the one-loop beta functions for the SDW critical point,



$$\partial_\ell v = \frac{z_\tau g^2}{16\pi} \left[ 1 - \frac{4(N_c^2 - 1)}{\pi N_c N_f} v (h_1(v, c) + h_2(v, c)) \right], \quad (31)$$

$$\partial_\ell c = -\frac{z_\tau g^2 c}{16\pi v} \left[ 1 - \frac{4(N_c^2 - 1)}{\pi N_c N_f} v (h_1(v, c) - h_2(v, c)) \right], \quad (32)$$

$$\partial_\ell g = z_\tau g \left[ \frac{\epsilon}{2} - \frac{g^2}{32\pi v} \left( 1 + \frac{4(N_c^2 - 1)}{\pi N_c N_f} v (h_1(v, c) + h_2(v, c)) \right) + \frac{g^2 v h_3(v, c)}{8\pi^3 N_c N_f} \right], \quad (33)$$

$$\partial_\ell \chi_1 = z_\tau \chi_1 \left[ \left( \epsilon - \frac{g^2}{8\pi v} \right) - \left( \frac{N_c^2 + 7}{2\pi^2} \chi_1 + \frac{2N_c^2 - 3}{\pi^2 N_c} \chi_2 + \frac{3(N_c^2 + 3)}{2\pi^2 N_c^2} \frac{\chi_2^2}{\chi_1} \right) \right], \quad (34)$$

$$\partial_\ell \chi_2 = z_\tau \chi_2 \left[ \left( \epsilon - \frac{g^2}{8\pi v} \right) - \left( \frac{6}{\pi^2} \chi_1 + \frac{N_c^2 - 9}{\pi^2 N_c} \chi_2 \right) \right]. \quad (35)$$

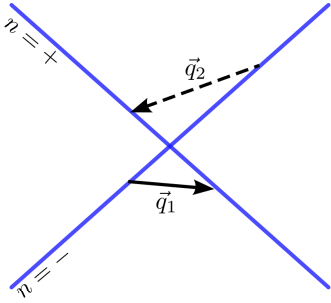


FIG. 4: For any momentum  $\vec{q} = (q_x, q_y)$  on the xy-plane, one can always find particle-hole pairs with zero energy across two patches of Fermi surface near hot spots. Since the fermionic dispersion is linear, the spectrum of particle-hole pair is independent of  $\vec{q}$ .

Now we explain the physical origin of each term in the beta functions based on the results obtained in Appendix A. The boson self energy in Fig. 3b is proportional to  $|\mathbf{Q}|^2$  and independent of  $\vec{q} = (q_x, q_y)$ . This is because a boson with any  $\vec{q}$  can be absorbed by a particle-hole pair on the Fermi surface (see Fig. 4), and the energy spectrum of particle-hole excitations is independent of  $\vec{q}$ . Vanishing  $Z_{5,1}$  and  $Z_{6,1}$  at the one-loop order, along with the negative sign of  $Z_{4,1}$  (the counter term and the quantum correction generated by integrating out high energy modes in the Wilsonian RG have opposite signs), leads to a weakened dependence of the dressed boson propagator on  $q_x, q_y$  relative to that of  $\mathbf{Q}$ . As a result,  $c_x$  and  $c_y$  are renormalized to smaller values. Because  $v = v_x/c_x$  and  $c = c_y/v_y$ , as defined in Eqs. (1) and (3), the suppression of  $c_x$  and  $c_y$  enhances  $v$  and suppresses  $c$ . This is shown in the first terms on the right hand side of Eqs. (31) and (32). The  $\mathbf{K}$  dependent term ( $Z_{1,1}$ ) in the fermion self energy in Fig. 3a similarly reduces  $v_x$  and  $v_y$ . This reduces  $v$  and enhance  $c$  as is shown in the second terms ( $\propto h_1$ ) on the right hand side of Eqs. (31) and (32). Fig. 3a also directly renormalizes the Fermi velocity through  $Z_{2,1}, Z_{3,1}$ . The spin fluctuations mix electrons from different hot spots. This reduces the angle between the Fermi velocities at the hot spots connected by  $\vec{Q}_{ord}$ ,

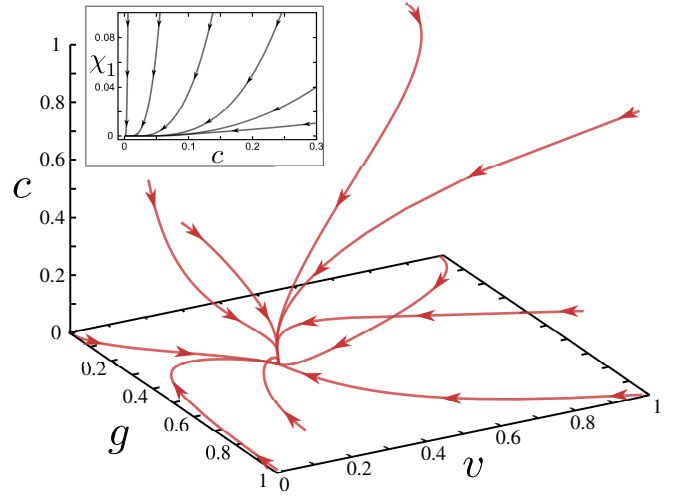


FIG. 5: Projection of the RG flow in the space of  $(g, v, c)$  for  $N_c = 2, N_f = 1$  and  $\epsilon = 0.01$ . The arrows point towards decreasing energy. An IR fixed point given by Eq. (43) exists on the  $(g, v)$  plane with  $c = 0$ . (Inset) Projection of the RG flow in the  $(\chi_1, c)$  plane.  $c$  ( $\chi_1$ ) flows to zero logarithmically (algebraically).

thereby improving the nesting between the hot spots. As  $v_x$  and  $v_y$  are renormalized to smaller and larger values respectively,  $v$  and  $c$  are suppressed. This is embodied in the third terms ( $\propto h_2$ ) in the expressions for  $\partial_\ell v$  and  $\partial_\ell c$ .

The beta function for the Yukawa vertex includes two different contributions. The second ( $\propto 1$ ), third ( $\propto h_1$ ) and fourth ( $\propto h_2$ ) terms on the right hand side of Eq. (33) are the contributions from the boson and fermion self energies which alter the scaling dimensions of spacetime and the fields. The contributions from the self-energies weaken the interaction at low energies because the virtual excitations in Figs. 3a, 3b screens the interaction. This is reflected in the negative contributions to the beta function. The last term ( $\propto h_3$ ) in Eq. (33) is the vertex correction ( $Z_{7,1}$ ) shown in Fig. 3c. Unlike the contributions from the self-energies, the vertex correction anti-screens the interaction, which tends to make the interac-

tion stronger. The anti-screening is attributed to the fact that the SDW vertices anti-commute on average in the sense,

$$\sum_{a=1}^{N_c^2-1} \tau^a \tau^b \tau^a = -\frac{2}{N_c} \tau^b. \quad (36)$$

This is analogous to the anti-screening effect which results in the asymptotic freedom in non-abelian gauge theories. The anti-screening effect also has a significant impact at the two-loop order as will be discussed in Sec. IV B.

The beta functions for  $\chi_i$  can be understood similarly. The second terms in the Eqs. (34) and (35) are the contributions from the boson self-energy. Rest of the terms in these equations are the standard vertex corrections ( $Z_{8,1}$ ,  $Z_{9,1}$ ) from Fig.

3d. We note that Fig. 3e does not contribute to the beta functions, because it is UV finite at  $d = 3$  [37].

In Fig. 5 we plot the one-loop RG flow of the four parameters,  $(g, v, c, \chi_1 = u_1/c)$  for  $N_c = 2$  and  $N_f = 1$ . Here we set  $u_2 = 0$ . The RG flow shows the presence of a stable IR fixed point with vanishing  $c$  and  $\chi_1$ . In order to find the analytic expression of the couplings at the fixed point for general  $N_c$  and  $N_f$ , we expand  $h_i(v, c)$  to the linear order in  $c$  with  $v \sim 1$ ,

$$\begin{aligned} h_1(v, c) &= \frac{\pi}{2} - 2c + \mathcal{O}(c^2), \quad h_2(v, c) = 2c + \mathcal{O}(c^2), \\ h_3(v, c) &= \frac{2\pi^2}{v(1+v)} - \frac{4\pi}{v}c + \mathcal{O}(c^2). \end{aligned} \quad (37)$$

In the small  $c$  limit, the beta functions become

$$\partial_\ell v = \frac{z_\tau}{16\pi} g^2 \left[ 1 - \frac{2(N_c^2 - 1)}{N_c N_f} v \right], \quad (38)$$

$$\partial_\ell c = -\frac{z_\tau}{16\pi} \frac{g^2 c}{v} \left[ \left( 1 - \frac{2(N_c^2 - 1)}{N_c N_f} v \right) + \frac{16(N_c^2 - 1)}{\pi N_c N_f} v c \right], \quad (39)$$

$$\partial_\ell g = \frac{1}{2} z_\tau g \left[ \epsilon - \frac{g^2}{16\pi v} \left\{ 1 + \frac{2(N_c^2 - 1)}{N_c N_f} v - \frac{8v}{N_c N_f (1+v)} \right\} \right], \quad (40)$$

$$\partial_\ell \chi_1 = z_\tau \chi_1 \left[ \left( \epsilon - \frac{g^2}{8\pi v} \right) - \left( \frac{N_c^2 + 7}{2\pi^2} \chi_1 + \frac{2N_c^2 - 3}{\pi^2 N_c} \chi_2 + \frac{3(N_c^2 + 3)}{2\pi^2 N_c^2} \frac{\chi_2^2}{\chi_1} \right) \right], \quad (41)$$

$$\partial_\ell \chi_2 = z_\tau \chi_2 \left[ \left( \epsilon - \frac{g^2}{8\pi v} \right) - \left( \frac{6}{\pi^2} \chi_1 + \frac{N_c^2 - 9}{\pi^2 N_c} \chi_2 \right) \right]. \quad (42)$$

Although the anti-screening vertex correction (the last term in Eq. (40)) tends to enhance the coupling, the screening from the self-energies is dominant for any  $N_c \geq 2$ . As a result,  $g$  is stabilized at a finite value below three dimensions. The stable one-loop fixed point is given by

$$\begin{aligned} v_* &= \frac{N_c N_f}{2(N_c^2 - 1)}, \\ g_*^2 &= \frac{4\pi N_c N_f}{(N_c^2 - 1)} \aleph(N_c, N_f) \epsilon, \\ c_* &= 0, \\ \chi_{1*} &= \chi_{2*} = 0, \end{aligned} \quad (43)$$

where

$$\aleph(N_c, N_f) = \frac{2(N_c^2 - 1) + N_c N_f}{2(N_c^2 - 3) + N_c N_f}. \quad (44)$$

At the one-loop order, the dynamical critical exponent  $z_\tau = 1 + \frac{\aleph(N_c, N_f)}{2} \epsilon$  becomes greater than one, while  $z_x$  retains its classical value. However,  $z_x$  deviates from one at the two-loop order as will be shown later. It is remarkable that the quantum scaling dimensions of the quartic vertices  $(\epsilon - g^2/8\pi v)$  be-

come negative at the fixed point, resulting in their irrelevance even below three dimensions. This is due to the fact that the effective spacetime dimension,  $d_{eff} = (2 - \epsilon)z_\tau + z_x + 1$ , at the one-loop fixed point is greater than  $d = 4 - \epsilon$  of the classical theory. In this sense the upper critical dimension for the quartic vertices is pushed down below  $3 - \epsilon$  at the interacting fixed point [10, 11].

We note that Eq. (43) is the fixed point of the full beta functions in Eqs. (31) - (35), because the truncation of higher order terms in Eq. (37) becomes exact in the small  $c$  limit. Besides the Gaussian and stable non-Fermi liquid fixed points, there exist two unstable interacting fixed points as listed in Table I. At the fixed point II, the fermions are decoupled from the bosons, and the dynamics of the boson is controlled by the Wilson-Fisher fixed point. Here  $g$  and  $\chi_2$  are relevant perturbations. The other fixed point (III) is realized at  $(\chi_1, \chi_2) = \left( -\frac{2\pi^2(\aleph(N_c, N_f) - 1)}{N_c^2 + 7} \epsilon, 0 \right)$  with the same values of  $g, c, v$  as in Eq. (43). A deviation of  $\chi_1$  from III is the relevant perturbation, which takes the flow either towards the stable fixed point (IV) at the origin of  $(\chi_1, \chi_2)$ -plane, or towards strong coupling where  $\chi_1$  becomes large and negative. The full RG flow in the  $(\chi_1, \chi_2)$ -plane at fixed  $g$  and  $v$  is shown in Fig. 6.

#	$\chi_1$	$\chi_2$	$g$	Relevant deformation	State
I	0	0	0	$g, \chi_1, \chi_2$	Free fermion and boson
II	$\frac{2\pi^2\epsilon}{N_c^2 + 7}$	0	0	$g, \chi_2$	Free fermion + Wilson-Fisher
III	$-\frac{2\pi^2(\aleph(N_c, N_f) - 1)\epsilon}{N_c^2 + 7}$	0	$g_*$	$\chi_1$	Unstable non-Fermi liquid
IV	0	0	$g_*$	None	Stable non-Fermi liquid

TABLE I: The four fixed points in the three dimensional space of couplings.  $g_*$  is defined in Eq. (43). The penultimate column lists the couplings that need to be tuned to reach the fixed point (besides the mass that has been tuned to reach the critical point).

We now focus on the stable fixed point (IV), which is realized at the critical point without further fine tuning. At the fixed point the electron and boson propagators satisfy the scaling forms,

$$G_{l,m}(k) = \frac{1}{|k_y|^{1-2\tilde{\eta}_\psi}} \mathcal{G}_{l,m} \left( \frac{k_x}{|k_y|^{z_x}}, \frac{\mathbf{K}}{|k_y|^{z_\tau}} \right), \quad (45)$$

$$D(q) = \frac{1}{|q_y|^{2-2\tilde{\eta}_\phi}} \mathcal{D} \left( \frac{q_x}{|q_y|^{z_x}}, \frac{\mathbf{Q}}{|q_y|^{z_\tau}} \right). \quad (46)$$

The anomalous dimensions that dictate the scaling of the two-point functions are deduced from Eq. (12), and they are given by combinations of  $\eta_\psi$ ,  $\eta_\phi$ ,  $z_\tau$  and  $z_x$ .

$$\begin{aligned} \tilde{\eta}_\psi &= \frac{2z_\tau + z_x - 3}{2} + \eta_\psi, \\ \tilde{\eta}_\phi &= \frac{2z_\tau + z_x - 3}{2} + \eta_\phi. \end{aligned} \quad (47)$$

At the one-loop order,  $\tilde{\eta}_\psi = 0$  and  $\tilde{\eta}_\phi = 0$ .  $\mathcal{G}_{l,m}(x, y)$  and  $\mathcal{D}(x, y)$  are universal functions of the dimensionless ratios of momentum and frequency. Due to the non-trivial dynamical critical exponent, the single-particle excitations are not well-defined, and the electrons near the hot spots become non-Fermi liquid below three dimensions. Since at one-loop order the critical exponents are solely determined by the Yukawa coupling and the velocities, the unstable fixed point III is also a non-Fermi liquid.

The velocity  $c$  which measures the boson velocity along the direction of the ordering vector with respect to the Fermi velocity flows to zero logarithmically. The vanishing velocity leads to enhanced fluctuations of the collective mode at low energies, which can make higher-loop corrections bigger than naively expected. This can, in principle, pose a serious threat to a controlled expansion. In order to see whether the perturbative expansion is controlled beyond one-loop, one first needs to understand how higher-loop corrections change the flow of  $c$ . In the following two sub-sections, we show that  $c$  flows to a non-zero value which is order of  $\epsilon^{1/3}$  due to a two-loop correction, and the perturbative expansion is controlled.

## B. Beyond One Loop

### 1. Estimation of general diagrams

The vanishing boson velocity at the one-loop fixed point can enhance higher order diagrams which are nominally suppressed by the small coupling  $g^2 \sim \epsilon$ . A  $L$ -loop diagram with  $V_g$  Yukawa vertices and  $V_u$  quartic vertices takes the form of

$$\begin{aligned} F(p_i; v, c, g, \chi; \epsilon, V_g, V_u, L) &\propto g^{V_g} \chi^{V_u} c^{V_u} \\ &\times \int \left[ \prod_{i=1}^L dp'_i \right] \prod_{l=1}^{I_f} \left( \frac{1}{\mathbf{\Gamma} \cdot \mathbf{K}_l + \gamma_{d-1} [v k_{l,x} + n_l k_{l,y}]} \right) \\ &\times \prod_{m=1}^{I_b} \left( \frac{1}{|\mathbf{Q}_m|^2 + q_{m,x}^2 + c^2 q_{m,y}^2} \right). \end{aligned} \quad (48)$$

Here  $p_i$  ( $p'_i$ ) are external (internal) momenta, and  $k_i$  and  $q_i$  are linear combinations of  $p_i$  and  $p'_i$ .  $\chi$  represents either  $\chi_1$  or  $\chi_2$ , whose difference is not important for the current purpose.  $I_f$  and  $I_b$  are the numbers of the internal electron and boson propagators, respectively.  $n_l$  is either  $+$  or  $-$  depending on the hot spot index carried by the  $l$ -th electron propagator.

When  $c$  is zero, some loop integrations can diverge as the dependence on  $q_y$  drops out in the boson propagator. This happens in the *bosonic loops*, which are solely made of boson propagators. For example,  $y$ -component of the internal momentum in Fig. 3d is unbounded at  $c = 0$ . For a small but nonzero  $c$ , the UV divergence is cut-off at a scale proportional to  $1/c$ . As a result, the diagram is enhanced by  $1/c$ . This is why  $Z_{8,1}$  and  $Z_{9,1}$  in Eq. (28) is order of  $\chi$  not  $\chi c$ .

Such enhancement can also arise if bosonic loops are formed out of dressed vertices and dressed propagators. Let us first consider the case with dressed vertices. Superficially, the diagram in Fig. 7 does not have any boson loop. However, the fermion loop can be regarded as a quartic boson vertex which is a part of a bosonic loop. Since the quartic vertex is dimensionless at the tree-level in 3 dimensions, it is not suppressed at large momentum. Therefore, the diagram can exhibit an enhancement of  $1/c^2$  as the boson propagators lose dispersion in the small  $c$  limit.

Similarly, boson loops made of dressed boson propagators can exhibit enhancements. However, the situation is a bit more

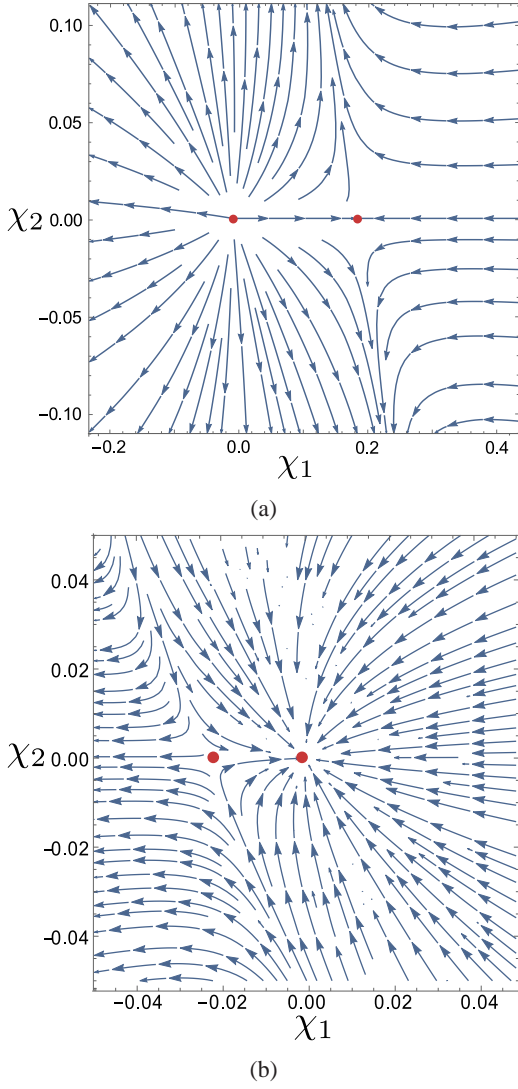


FIG. 6: RG Flow in the  $\chi_1 - \chi_2$  plane with  $N_c = 4$ ,  $N_f = 1$ , and  $\epsilon = 0.2$ . (a) In the subspace of  $g = 0$ , there are two unstable fixed points at  $\chi_1 = 0$  and  $\chi_1 \sim \epsilon$  with  $\chi_2 = 0$ . The former is the Gaussian fixed point, while the latter is the Wilson-Fisher fixed point. (b) In the subspace of  $g = g_*$  and  $v = v_*$ , there exist an unstable non-Fermi liquid at  $\chi_1 \sim -\epsilon$ , and a stable non-Fermi liquid at  $\chi_1 = 0$  with  $\chi_2 = 0$ . The arrows in both plots point towards increasing length scale, and the (red) dots indicate the fixed points.

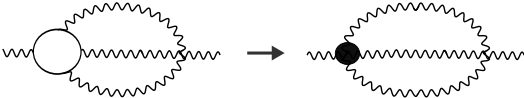


FIG. 7: A three-loop diagram which can be enhanced by upto  $1/c^2$ . This diagram does not include any loop that is solely made of boson propagators. Nonetheless, this can exhibit an enhancement in powers of  $1/c$  as the fermionic loop plays the role of a bosonic quartic vertex (represented by shaded circles), which is not suppressed at large momentum.



FIG. 8: Examples of (amputated) boson self-energy which can potentially diverge with order of 1 coefficient in the large  $q_y$  limit.

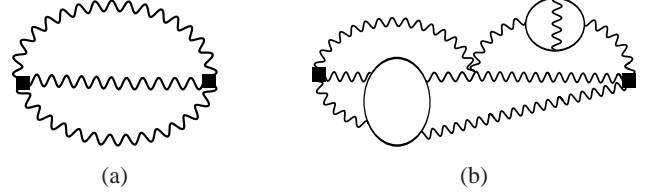


FIG. 9: Examples of (amputated) boson self-energy diagrams whose dependences on  $q_y$  are suppressed by  $c$ . This can be seen from that fact that the external momentum can be directed to go through only boson propagators which are independent of  $y$ -momentum in the small  $c$  limit. Consequently, the self-energy depends on  $q_y$  only through  $cq_y$ .

complicated in this case. Since boson self-energy has scaling dimension 2, it can diverge quadratically in the momentum that flows through the self-energy. Therefore, there can be an additional enhancement of  $1/c^2$  in the small  $c$  limit because the typical  $y$ -component of internal momentum is order of  $1/c$  in the boson loops. In order to account for the additional enhancements from the boson self-energy more precisely, it is convenient to divide diagrams for boson self-energy into two groups. The first group includes those diagrams which diverge in the large  $q_y$  limit with order of 1 coefficient as  $c$  goes to zero. Potentially, the diagrams in Fig. 8 have un-suppressed dependence on  $q_y$  because the external momentum must go through at least one fermion propagator whose dispersion is not suppressed in the small  $c$  limit. Each boson self-energy of the first kind in bosonic loops contributes a factor of atmost  $1/c^2$ . The second group includes those diagrams that are either independent of  $q_y$  for any  $c$ , or become independent of  $q_y$  as  $c$  goes to zero. For example, the one-loop self-energy in Fig. 3b is independent of  $q_y$ . The diagrams in Fig. 9 depend on  $q_y$  through the combination  $cq_y$  because the external momentum can be directed to go through only boson propagators which are independent of  $y$ -momentum in the small  $c$  limit. Therefore, the self-energies in the second group do not contribute an additional enhancement of  $1/c$ .

Owing to the aforementioned reasons a general diagram can be enhanced *at most* by a factor of  $c^{-L_b - 2N_{\Pi}}$ , where  $L_b$  is the number of loops solely made of bosonic propagators once fermion loops are replaced by the corresponding effective  $\phi^{2n}$  vertices, and  $N_{\Pi}$  is the total number of boson self-energy of

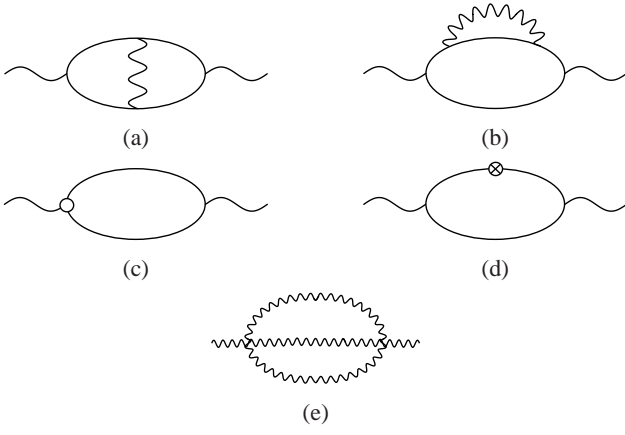


FIG. 10: The diagrams for the two-loop boson self energy. The small circles in (c) and (d) denote the one-loop counter terms.

the first kind in bosonic loops. Therefore, we estimate the upper bound for the magnitude of general higher-loop diagrams to be

$$F(p_i; v, c, g, \chi; \epsilon, V_g, V_u, L, L_b, N_\Pi) = \left(\frac{g^2}{c}\right)^{V_g/2} \chi^{V_u} c^{(E-2)/2 + (L-L_b-2N_\Pi)} f(p_i; v, c; \epsilon, L), \quad (49)$$

where we have used the relation  $L = (V_g + 2V_u + 2 - E)/2$  with  $E$  being the number of external legs. The function  $f(p_i; v, c; \epsilon, L)$  is regular in the small  $c$  limit. We emphasize that Eq. (49) is an upper bound in the small  $c$  limit. The actual magnitudes may well be smaller by positive powers of  $c$ . For example, Fig. 10a is nominally order of  $g^4/c$  in the small  $c$  limit according to Eq. (49). However, an explicit computation shows that it is order of  $g^4$ . Currently, we do not have a full expression for the actual magnitudes of general diagrams in the small  $c$  limit. Our strategy here is to use the upper bound, which is sufficient to show that the perturbative expansion is controlled.

## 2. Two-loop correction

The ratio  $g^2/c$  which diverges at the one-loop fixed point may spoil the control of the perturbative expansion. However, such a conclusion is premature because higher-loop diagrams that are divergent at the one-loop fixed point can feed back to the flow of  $c$  and stabilize it at a nonzero value. As long as  $c$  is not too small, higher-loop diagrams can be still suppressed. In order to include the leading quantum correction to  $c$ , we first focus on the two-loop diagrams for the boson self-energy shown in Fig. 10.

An explicit calculation in Appendix A 2 shows that only Fig. 10a renormalizes  $c$  in the limit  $c \rightarrow 0$ . Other two-loop diagrams are suppressed by additional factors of  $c$ ,  $g$ , or  $\chi_i$  compared to Figs. 10a. Because stabilization of  $c$  at a non-

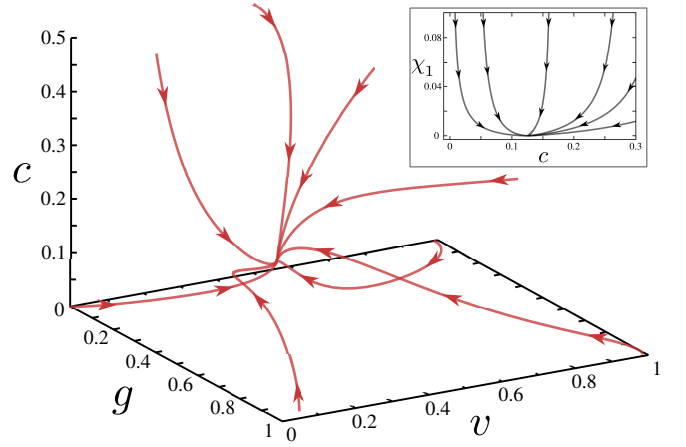


FIG. 11: Projection of the RG flow in the  $(g, v, c)$  space for  $N_c = 2$ ,  $N_f = 1$  and  $\epsilon = 0.01$ . The fixed point in Fig. 5 is modified by the two-loop correction (Fig. 10a) such that  $c$  flows to a non-zero value as shown in Eq. (57). (Inset) Projection of the RG flow in the  $(\chi_1, c)$  plane. Although  $\chi_1$  still flows to zero,  $c$  does not.

zero value can occur only through two or higher loop effect, the non-zero value of  $c$  must be order of  $\epsilon^b$  with  $b > 0$ . The two-loop diagram in Fig. 10a is proportional to  $g^4 q_y^2$ , which is strictly smaller than the upper bound in Eq. (49) by a factor of  $c$ . Its contribution to  $Z_{6,1}$  is given by

$$Z_{6,1} = -\frac{8}{N_c N_f} \frac{g^4}{v^2 c^2} (h_6(v) + \mathcal{O}(c)), \quad (50)$$

where  $h_6(v)$  is defined in Eq. (A35). The extra factor of  $1/c^2$  in Eq. (50) originates from the fact that  $Z_{6,1}$  is the multiplicative renormalization to the boson kinetic term,  $c^2 q_y^2$ . Since the quantum correction from the two-loop diagram does not vanish in the small  $c$  limit, it is relatively large compared to the vanishingly small classical action  $c^2 q_y^2$ . Because Fig. 10a generates a positive kinetic term at low energy, it stabilizes  $c$  at a nonzero value. The non-commuting nature of the SDW vertex in Eq. (36) is crucial for the stabilization of  $c$ . Without the anti-screening effect, Eq. (50) would come with the opposite sign, and  $c$  would flow to zero even faster by the two-loop effect. As we will see, the two-loop diagram indeed suppresses  $c$  in the CDW case, where there is no anti-screening effect.

The RG flow which includes the two-loop effect is shown in Fig. 11 for  $N_c = 2$  and  $N_f = 1$ .  $c$  flows to a small but non-zero value in the low energy limit, while the other three parameters flow to values that are similar to those obtained at the one-loop order.  $g/c$  becomes order of  $\epsilon^{1/6}$  at the fixed point as is shown in Fig. 12. To find the fixed point for general  $N_c$  and  $N_f$  analytically, we analyze the beta functions in the region where  $v \sim 1$  and  $0 < c \ll 1$ . The beta functions can be written as an expansion in  $g/c$ ,  $\chi_i$  and  $c$ ,

$$\partial_\ell \lambda = \lambda \sum_{l,m,n=0}^{\infty} J_{l,m,n}^{(\lambda)}(v, \epsilon) \left(\frac{g}{c}\right)^{2l} \chi_i^{m-1} c^{n-1}, \quad (51)$$



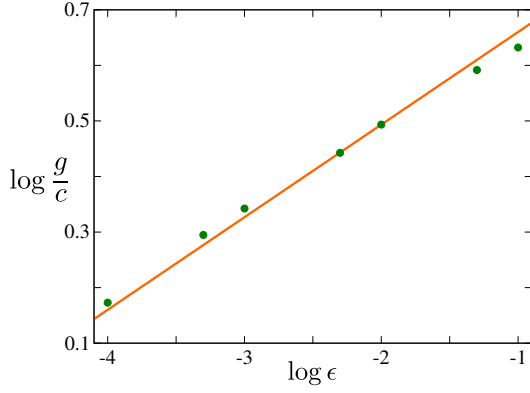


FIG. 12: The ratio  $g/c$  as a function of  $\epsilon$  obtained from the numerical solution of the full beta functions in the low energy limit for  $N_f = 1$  and  $N_c = 2$ . The filled circles are from the numerical solution of the beta functions, and the straight line is a fit,  $g/c = 6.7 \epsilon^{1/6}$ .

where  $\lambda$  represents a velocity or a coupling, and  $J_{l,m,n}^{(\lambda)}(v, \epsilon)$  are functions of  $v$  and  $\epsilon$ . From general considerations some  $J_{l,m,n}^{(\lambda)}(v, \epsilon)$  can be shown to be zero [59]. To  $\mathcal{O}((g/c)^4 c^2, \chi)$  in the small  $g/c, \chi, c$  limit, the beta functions are given by

$$\partial_\ell v = \frac{z_\tau}{16\pi} v \left[ \frac{g^2}{v} - \frac{2(N_c^2 - 1)}{N_c N_f} g^2 \right], \quad (52)$$

$$\partial_\ell c = -\frac{z_\tau}{16\pi} \frac{g^2 c}{v} \left[ \left( 1 - \frac{2(N_c^2 - 1)}{N_c N_f} v \right) + \frac{16(N_c^2 - 1)v}{\pi N_c N_f} \left( c - \frac{8\pi^2}{(N_c^2 - 1)} \frac{g^2 h_6(v)}{v^2 c^2} \right) \right], \quad (53)$$

$$\partial_\ell g = \frac{1}{2} z_\tau g \left[ \epsilon - \frac{g^2}{16\pi v} \left\{ 1 + \frac{2(N_c^2 - 1)}{N_c N_f} v - \frac{8v}{N_c N_f (1 + v)} \left( 1 - \frac{2}{\pi} (1 + v) c \right) \right\} \right], \quad (54)$$

$$\partial_\ell \chi_1 = z_\tau \chi_1 \left[ \left( \epsilon - \frac{g^2}{8\pi v} - \frac{8}{N_c N_f} \frac{g^4 h_6(v)}{v^2 c^2} \right) - \left( \frac{N_c^2 + 7}{2\pi^2} \chi_1 + \frac{2N_c^2 - 3}{\pi^2 N_c} \chi_2 + \frac{3(N_c^2 + 3)}{2\pi^2 N_c^2} \frac{\chi_2^2}{\chi_1} \right) \right], \quad (55)$$

$$\partial_\ell \chi_2 = z_\tau \chi_2 \left[ \left( \epsilon - \frac{g^2}{8\pi v} - \frac{8}{N_c N_f} \frac{g^4 h_6(v)}{v^2 c^2} \right) - \left( \frac{6}{\pi^2} \chi_1 + \frac{N_c^2 - 9}{\pi^2 N_c} \chi_2 \right) \right]. \quad (56)$$

We note that  $J_{1,1,1}^{(c)}(v, \epsilon), J_{1,1,2}^{(c)}(v, \epsilon), J_{2,1,0}^{(c)}(v, \epsilon), J_{2,1,1}^{(c)}(v, \epsilon), J_{2,1,2}^{(c)}(v, \epsilon) = 0$  in Eq. (53). This underscores the fact that the actual magnitudes of the diagrams can be smaller than Eq. (49) which is only the upper bound.

In the small  $c$  limit, only the flows of  $c$  and  $\chi_i$  are affected by the two-loop diagram through the fourth term in Eq. (53) and the third terms in Eqs. (55) and (56), respectively. While  $c$  tends to decrease under the one-loop effect, the two-loop correction enhances  $c$  due to the anti-screening produced by the vertex correction. These opposite tendencies eventually balance each other to yield a stable fixed point for  $c$ . At the fixed point of  $v_* \sim \mathcal{O}(1)$  and  $g_*^2 \sim \mathcal{O}(\epsilon)$ , the beta function for  $c$  is proportional to  $-c + r\epsilon/c^2$  with a constant  $r > 0$ , such that  $c$  flows to  $\mathcal{O}(\epsilon^{1/3})$  in the low energy limit. This confirms that  $g/c$  is  $\mathcal{O}(\epsilon^{1/6})$  at the fixed point.

The RG flow in the  $\chi_1 - \chi_2$  plane resembles Fig. 6 for small  $\epsilon$ , and the  $\chi_i$ 's remain irrelevant at the fixed point. The two-loop diagrams in Fig. 13 will generate non-zero quartic couplings which are at most order of  $\mathcal{O}(g^6/c^2)$  in the beta function for  $\chi_i$ . This is no longer singular because  $g^2 \sim \epsilon$

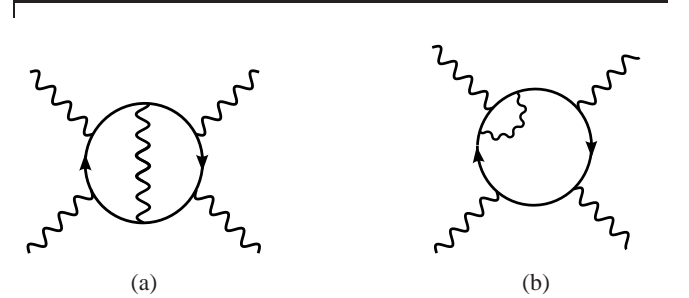


FIG. 13: The leading two-loop diagrams that generate bosonic quartic interaction.

and  $c \sim \epsilon^{1/3}$  at the fixed point. If the leading order term of  $\mathcal{O}(g^6/c^2)$  survives, the beta functions for  $\chi_i$  has the form of  $-\epsilon\chi_i + r'g^6/c^2$  with a constant  $r'$ . This suggests that  $\chi_i$  is at most  $\mathcal{O}(\epsilon^{4/3})$  at the fixed point. Other two-loop diagrams and higher-loop diagrams are suppressed by additional powers of  $\epsilon^{1/3}$  compared to the one-loop diagrams and the two-loop diagram in Fig. 10a, which are already included. Therefore,



the two-loop effect modifies the fixed point as

$$\begin{aligned}
v_* &= \frac{N_c N_f}{2(N_c^2 - 1)} + \mathcal{O}(\epsilon^{1/3}), \\
g_*^2 &= \frac{4\pi N_c N_f}{(N_c^2 - 1)} \aleph(N_c, N_f) \left[ \epsilon - \frac{16}{N_c^2 - 1} \left( \frac{2 \aleph^4(N_c, N_f) h_6(v_*)}{N_c N_f} \right)^{1/3} \epsilon^{4/3} \right] + \mathcal{O}(\epsilon^{5/3}), \\
c_* &= 4\pi \left[ \frac{2 \aleph(N_c, N_f)}{N_c N_f} h_6(v_*) \right]^{1/3} \epsilon^{1/3} + \mathcal{O}(\epsilon^{2/3}), \\
\chi_{i,*} &= \mathcal{O}(\epsilon^{4/3}).
\end{aligned} \tag{57}$$

It is noted that  $\mathcal{O}(\epsilon^\alpha)$  in the above equations represent the upper bounds of the sub-leading terms. The actual sub-leading terms may be smaller than the upper bound. For example, the actual sub-leading correction to  $v_*$  is  $\mathcal{O}(\epsilon^{2/3})$  because the  $\mathcal{O}(c)$  term in  $h_1(v, c) + h_2(v, c)$  is zero (see Eq. (37)).

Eqs. (17)-(20) along with Eq. (49) implies that the anomalous dimensions at the fixed point can be expressed as

$$\Delta = \sum_{l,m,n=0} A_{l,m,n} \left( \frac{g_*}{c_*} \right)^{2l} \chi_*^m c_*^n, \tag{58}$$

where  $\Delta$  represents either  $z_\tau - 1$ ,  $z_x - 1$ ,  $\eta_\psi$ , or  $\eta_\phi$ , and  $A_{l,m,n}$  are constants with  $A_{0,0,n} = 0$ . Using the expressions of the parameters at the fixed point (Eq. (57)), we compute the critical exponents up to order  $\epsilon^{4/3}$ ,

$$\begin{aligned}
z_\tau &= 1 + \frac{\aleph(N_c, N_f)}{2} \epsilon \\
&\quad - 8 \left( 2 + \frac{\aleph(N_c, N_f)}{N_c^2 - 1} \right) \left( \frac{2 \aleph^4(N_c, N_f)}{N_c N_f} h_6(v_*) \right)^{1/3} \epsilon^{4/3}, \\
z_x &= 1 - 16 \left( \frac{2 \aleph^4(N_c, N_f)}{N_c N_f} h_6(v_*) \right)^{1/3} \epsilon^{4/3}, \\
\tilde{\eta}_\psi &= 4 \left( \frac{2 \aleph^4(N_c, N_f)}{N_c N_f} h_6(v_*) \right)^{1/3} \epsilon^{4/3}, \\
\tilde{\eta}_\phi &= 16 \left( \frac{2 \aleph^4(N_c, N_f)}{N_c N_f} h_6(v_*) \right)^{1/3} \epsilon^{4/3}.
\end{aligned} \tag{59}$$

The fixed point value of  $\chi_{i,*}$  does not affect the critical exponents up to  $\mathcal{O}(\epsilon^{4/3})$  because a single  $\phi^4$  vertex does not contribute to any of the nine counter terms. Because  $z_x$  differs from one at the fixed point, the system develops an anisotropy in the  $(k_x, k_y)$  plane.

### C. Control of the perturbative expansion

In the previous subsection, we incorporated one particular two-loop diagram which stabilizes the boson velocity at

a non-zero value in order to compute the critical exponents to the order of  $\epsilon^{4/3}$ . A natural question is whether it is safe to ignore other two-loop diagrams, and more generally whether the perturbative expansion is under control for small  $\epsilon$ . From Eq. (57) we note that  $g^2 \sim c^3$  at the fixed point, and Eq. (49) can be expressed in terms of  $c$  and  $\chi$ ,

$$\begin{aligned}
&F(p_i; v, c, g, \chi; \epsilon, V_g, V_u, L, L_b, N_\Pi) \\
&= \chi^{V_u} c^{(E-2)/2 + (L-L_b) + (V_g - 2N_\Pi)} f'(p_i; v, c; \epsilon, L).
\end{aligned} \tag{60}$$

Here  $f'(p_i; v, c; \epsilon, L)$  is finite in the small  $c$  limit. The exponents of  $\chi$ ,  $c$  are non-negative because  $L \geq L_b$  and  $V_g > 2N_\Pi$ . The latter inequality follows from the fact that any diagram for boson self-energy of the first kind must contain at least four Yukawa vertices. For a fixed  $E$ , new vertices cannot be added without increasing either  $V_u$ ,  $(L - L_b)$ , or  $(V_g - 2N_\Pi)$ . Therefore, Eq. (60) implies that quantum corrections are systematically suppressed by powers of  $c \sim \epsilon^{1/3}$  and  $\chi \lesssim \epsilon^{4/3}$  as the number of loops increases, and there exist only a finite number of diagrams at each order. This shows that other two-loop diagrams and higher-loop diagrams are indeed sub-leading, and they do not modify the critical exponents in Eq. (59) up to the order of  $\epsilon^{4/3}$ .

Sub-leading terms come in two ways. The first is from the  $c$ -expansions of  $h_i(v, c)$  defined in Eq. (37). The second is from higher-loop diagrams. For  $Z_{n,1}$  with  $n = 1, 2, 3, 7$ , two-loop diagrams are suppressed at least by  $\epsilon^{5/3}$  according to Eq. (60) because  $(L - L_b) \geq 1$  and  $V_g - 2N_\Pi \geq 4$  for the fermion self energy and the Yukawa vertex correction.  $\mathcal{O}(c^2)$  terms in the expansion of  $h_i(v, c)$  from the one-loop diagrams are also at most order of  $\epsilon^{5/3}$ . For  $Z_{4,1}$ , the one-loop diagram does not contain any sub-leading term in  $c$ . According to Eq. (60), higher-loop contributions to  $Z_{4,1}$  are at most order of  $g^4/c \sim \epsilon^{5/3}$ . As noted earlier, the first non-vanishing contributions to  $Z_{5,1}$  and  $Z_{6,1}$  arise at the two-loop order. In Appendix A 2, we show that the leading order term in  $Z_{5,1}$  is at most order of  $g^4 c \sim \epsilon^{7/3}$ . In contrast, Eq. (50) shows that the leading order term in  $Z_{6,1}$  is  $g^4/c^2 \sim \epsilon^{4/3}$  which is already included. The sub-leading terms are suppressed by  $c, g^2/c^2 \sim \epsilon^{1/3}$ . As discussed below Eq. (56),  $\chi_i$  are at most  $\mathcal{O}(\epsilon^{4/3})$

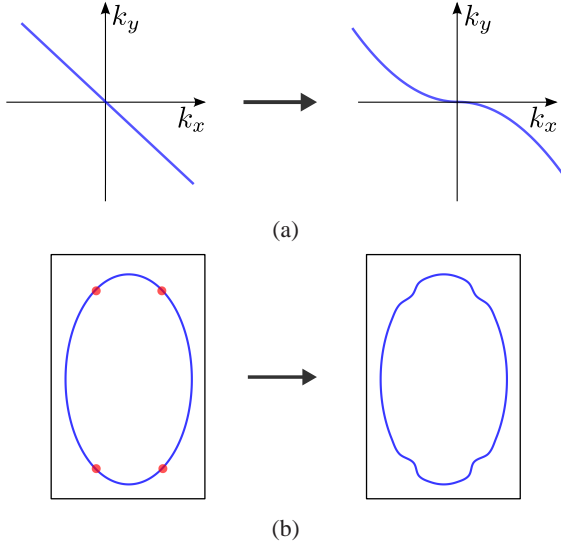


FIG. 14: (a) The patches of Fermi surface near the hot spots are deformed into a universal non-analytic curve. (b) The hot spots become algebraically nested near the hot spots.

from two-loop contributions. However,  $\chi_i \sim \epsilon^{4/3}$  can not affect the critical exponents up to  $\mathcal{O}(\epsilon^{4/3})$  because a single quartic vertex only renormalizes boson mass. Thus the critical exponents in Eq. (59) are accurate up to  $\mathcal{O}(\epsilon^{4/3})$ .

It is interesting to note that the perturbative expansion is not simply organized by the number of loops. Instead, one has to perform an expansion in terms of the couplings and the boson velocity together. There are notable consequence of this unconventional expansion. First, the perturbative expansion is in power series of  $\epsilon^{1/3}$ . Second, not all diagrams at a given loop play the same role; only one two-loop diagram (Fig. 10a) is important for the critical exponents to the order of  $\epsilon^{4/3}$ .

#### D. Physical Properties

In this section we discuss the physical properties of the non-Fermi liquid state that is realized at the SDW critical point. The anomalous dimension of  $k_x$  implies that the Fermi surface near the hot spots are deformed into a universal curve,

$$k_y \sim \text{sgn}(k_x) |k_x|^{1/z_x} \quad (61)$$

as is illustrated in Fig. 14. The algebraic nesting of the Fermi surface near the hot spots is in contrast to the  $C_4$ -symmetric case, where the emergent nesting is only logarithmic such that  $k_y \sim k_x / (\ln k_x)$  [21, 26, 37]. The electronic spectral function at the hot spot scales with frequency as

$$\mathcal{A}_{l,m}(\omega) \sim \frac{1}{\omega^{(1-2\tilde{\eta}_\psi)/z_\tau}}, \quad (62)$$

and the dynamical spin structure factor at momentum  $\vec{Q}_{ord}$ ,

$$\mathcal{S}(\omega) \sim \frac{1}{\omega^{(2-2\tilde{\eta}_\phi)/z_\tau}}. \quad (63)$$

As one moves away from the hot spots or the ordering vector in the  $x$  ( $y$ ) directions, the electron spectral function and the spin structure factor will exhibit incoherent peak at frequency  $\omega \sim |k_x|^{z_\tau/z_x}$  and  $\omega \sim |k_y|^{z_\tau}$  depending on the direction of momentum. In principle, all exponents  $z_\tau, z_x, \tilde{\eta}_\psi, \tilde{\eta}_\phi$  can be determined from the angle resolved photoemission and inelastic neutron scattering experiments. In Table II, we list the exponents at the fixed point for  $(N_c, N_f) = (2, 1)$  and  $(3, 1)$ . It is noted that  $z_x$  becomes smaller than one below three dimensions, which is consistent with the intuition that the interaction enhances nesting. However, the fact that  $z_x$  becomes negative for  $\epsilon = 1$  and  $N_c = 2$  should not be taken seriously, since higher order contributions need to be taken into account in two dimensions.

We also estimate the contribution of electrons near the hot spots to the specific heat and the optical conductivity following the work by Patel *et al.* for the  $C_4$ -symmetric model [38]. The scaling dimension of the free energy density  $\mathcal{F}$  is

$$[\mathcal{F}] = z_\tau(d-1) + 1 + z_x. \quad (64)$$

The current density  $\mathcal{J}_\mu$  has the dimension of  $[\mathcal{J}_\mu] = [\mathcal{F}] - [k_\mu]$ . Because  $k_x$  and  $k_y$  have different scaling dimensions, the two diagonal elements of the optical conductivity have different scaling dimensions,

$$\begin{aligned} [\sigma_{xx}] &= z_\tau(1-\epsilon) + 1 - z_x, \\ [\sigma_{yy}] &= z_\tau(1-\epsilon) + z_x - 1, \end{aligned} \quad (65)$$

at  $d = 3 - \epsilon$ . The contribution of the hot spot electrons obeys the hyperscaling because temperature or frequency provides a cut-off for the momentum along the Fermi surface. As a result, the size of Fermi surface does not enter in the scaling of the contributions from the hot spots. This is analogous to the phenomenon where the thermodynamic responses from inflection points obey the hyperscaling relation in non-Fermi liquids where Fermi surface is coupled with a  $\vec{Q}_{ord} = 0$  critical boson [23]. As a result, the hot spot contribution to the specific heat scales with temperature as

$$c^{hot} \sim T^{1-\epsilon+\frac{1+z_x}{z_\tau}}, \quad (66)$$

and the hot spot contributions to the optical conductivity scales with frequency as

$$\begin{aligned} \sigma_{xx}^{hot}(\omega) &\sim \omega^{1-\epsilon+\frac{1-z_x}{z_\tau}}, \\ \sigma_{yy}^{hot}(\omega) &\sim \omega^{1-\epsilon-\frac{1-z_x}{z_\tau}}. \end{aligned} \quad (67)$$

Because  $z_x < 1$ , the optical conductivity is greater along the ordering vector than the perpendicular direction at low frequency [60, 61]. We emphasize that the anisotropy in Eq. (67) arises from anisotropic spatial scaling, rather than anisotropic carrier velocity [62, 63]. Electrons away from the hot spots are expected to violate the hyperscaling, and contribute to the

$N_c$	$z_\tau$	$z_x$	$\tilde{\eta}_\psi$	$\tilde{\eta}_\phi$
2	$1 + \epsilon - 1.9 \epsilon^{4/3}$	$1 - 1.4 \epsilon^{4/3}$	$0.36 \epsilon^{4/3}$	$1.4 \epsilon^{4/3}$
3	$1 + 0.63 \epsilon - 0.68 \epsilon^{4/3}$	$1 - 0.63 \epsilon^{4/3}$	$0.16 \epsilon^{4/3}$	$0.63 \epsilon^{4/3}$

TABLE II: Fixed point values of the critical exponents for  $N_c = 2, 3$  with  $N_f = 1$ .

specific heat and the optical conductivity as  $c^{cold} \sim k_F T^{2-\epsilon}$  and  $\sigma^{cold} \sim k_F \omega^{-\epsilon}$ , where  $k_F$  is the size of Fermi surface. For small  $\epsilon$ , the contributions from cold electrons dominate the hot spot contributions.

Near three dimensions, there is no perturbative instability, and the anisotropic non-Fermi is stable. However, near two dimensions the non-Fermi liquid state can become unstable against other ordered phases. As far as the hot spot electrons are concerned, a charge density wave is the leading instability, followed by the  $d$ -wave pairing and pair density wave [37]. However, the order of leading instability can change due to cold electrons away from the hot spots, which favour zero-momentum pairing due to the lack of nesting.

## V. CHARGE DENSITY WAVE CRITICALITY

In this section, we discuss the low energy properties of the CDW critical point. Since many aspects are similar to the SDW case, we will highlight the differences between the two critical points. The main differences arise from the commuting versus non-commuting nature of the respective interaction vertices as is shown in Eqs. (1) and (2). It is analogous to the difference between the nematic and ferromagnetic critical points [64].

Since the CDW order parameter couples to the global  $U(1)$  charge, the interaction vertex is diagonal in both the spin and flavor space. One can also set  $\chi_2 = 0$  for any  $N_f$  and  $N_c$  since the two quartic vertices are equivalent. As derived in Appendix A, the counter terms resulting from the one-loop diagrams in Fig. 3 are

$$\begin{aligned}
Z_{1,1} &= -\frac{1}{4\pi^2 \tilde{N}_f} g^2 h_1(v, c), & Z_{2,1} &= \frac{1}{4\pi^2 \tilde{N}_f} g^2 h_2(v, c) \\
Z_{3,1} &= -\frac{1}{4\pi^2 \tilde{N}_f} g^2 h_2(v, c) & Z_{4,1} &= -\frac{1}{8\pi} \frac{g^2}{v}, \\
Z_{5,1} &= 0, & Z_{6,1} &= 0, \\
Z_{7,1} &= \frac{1}{8\pi^3 \tilde{N}_f} g^2 v h_3(v, c), & Z_{8,1} &= \frac{9}{2\pi^2} \chi_1,
\end{aligned} \tag{68}$$

where  $\tilde{N}_f = N_c N_f$ . Using the general expressions of the beta functions in section III, we obtain the one loop beta-functions for the CDW critical point. As in the SDW case, the boson velocity flows to zero in the low energy limit at the one-loop order. Therefore, we focus on the regime with small  $c$  where

the one-loop beta functions take the form,

$$\partial_\ell v = \frac{z_\tau}{16\pi} g^2 \left[ 1 - \frac{2v}{\tilde{N}_f} \right], \tag{69}$$

$$\partial_\ell c = -\frac{z_\tau}{16\pi} \frac{c}{v} g^2 \left[ \left( 1 - \frac{2v}{\tilde{N}_f} \right) + \frac{16 v c}{\pi \tilde{N}_f} \right], \tag{70}$$

$$\begin{aligned}
\partial_\ell g &= \frac{z_\tau}{2} g \left[ \epsilon - \frac{g^2}{16\pi v} \left\{ \left( 1 + \frac{2v}{\tilde{N}_f} \right) \right. \right. \\
&\quad \left. \left. + \frac{8v}{\tilde{N}_f(1+v)} \left( 1 - \frac{2}{\pi}(1+v)c \right) \right\} \right],
\end{aligned} \tag{71}$$

$$\partial_\ell \chi_1 = z_\tau \chi_1 \left[ \left( \epsilon - \frac{g^2}{8\pi v} \right) - \frac{9}{2\pi^2} \chi_1 \right]. \tag{72}$$

We note that the sign of  $Z_{7,1}$  for the CDW critical point is opposite to that of the SDW critical point. This is due to the fact that the three CDW vertices (identity matrix) that appear in Fig. 3c are mutually commuting, while the SDW vertices ( $SU(N_c)$  generators) are mutually anti-commuting as shown in Eq. (36). Consequently, the vertex correction screens the interaction at the CDW critical point in contrast to the SDW case. A stable one-loop fixed point arises at

$$\begin{aligned}
v_* &= \frac{\tilde{N}_f}{2}, \\
g_*^2 &= 4\pi \tilde{N}_f \frac{\tilde{N}_f + 2}{\tilde{N}_f + 6} \epsilon, \\
c_* &= 0, \\
\chi_{1,*} &= \frac{8\pi^2 \epsilon}{9(\tilde{N}_f + 6)}.
\end{aligned} \tag{73}$$

To the leading order in  $\epsilon$ , the critical exponents become

$$z_\tau = 1 + \frac{\tilde{N}_f + 2}{2(\tilde{N}_f + 6)} \epsilon, \quad z_x = 1, \quad \tilde{\eta}_\psi = 0 \quad \text{and} \quad \tilde{\eta}_\phi = 0. \tag{74}$$

Since the one-loop vertex correction screens the Yukawa interaction in Eq. (71), the Yukawa coupling is not strong enough to push the upper critical dimension for  $\chi_1$  below  $3 - \epsilon$ , in contrast to the SDW case. As a result,  $\chi_1$  remains non-zero at the one-loop fixed point below three dimensions. It is interesting to note that the weaker (better screened) Yukawa coupling makes it possible for the quartic coupling to be stronger at the

CDW critical point as compared to the SDW case.

We now investigate how the two-loop correction modifies the flow of  $c$ . The two-loop diagram in Fig. 10 leads to

$$Z_{5,1} = 0, \quad Z_{6,1} = \frac{8}{\tilde{N}_f} \frac{g^4}{v^2 c^2} h_6(v) \quad (75)$$

to the leading order in  $c$ . The modified beta functions for  $c$  and  $\chi_1$  are given by

$$\partial_\ell c = -\frac{z_\tau}{16\pi} \frac{c}{v} g^2 \left[ \left( 1 - \frac{2v}{\tilde{N}_f} \right) + \frac{16v}{\pi \tilde{N}_f} \left( c + \frac{8\pi^2 g^2 h_6(v)}{v^2 c^2} \right) \right], \quad (76)$$

$$\partial_\ell \chi_1 = z_\tau \chi_1 \left[ \left( \epsilon - \frac{g^2}{8\pi v} + \frac{8}{\tilde{N}_f} \frac{g^4}{v^2 c^2} h_6(v) \right) - \frac{9}{2\pi^2} \chi_1 \right]. \quad (77)$$

We note that the sign of  $Z_{6,1}$  in Eq. (75), which contributes the fourth term in Eq. (76) and the third term in Eq. (77), is opposite to that of  $Z_{6,1}$  for the SDW case in Eq. (50). This is again due to the commuting CDW vertices in contrast to the anti-commuting SDW vertices in Eq. (36). Therefore the two-loop diagram further reduces  $c$  for the CDW case, while it stops  $c$  from flowing to zero for the SDW case. Since Eq. (69) is not modified by the two-loop diagram,  $v$  flows to  $v_* = \tilde{N}_f/2$ , irrespective of how the other parameters flow, as long as  $c$  remains small. To understand the fate of the system in the low energy limit, it is useful to examine the flow of  $g, c, \chi_1$  with fixed  $v = v_*$ ,

$$\partial_\ell g = \frac{z_\tau}{2} g \left[ \epsilon - \frac{g^2}{4\pi \tilde{N}_f} \left\{ 1 + \frac{4}{\tilde{N}_f + 2} \left( 1 - \frac{\tilde{N}_f + 2}{\pi} c \right) \right\} \right], \quad (78)$$

$$\partial_\ell c = -\frac{32z_\tau}{\tilde{N}_f^3} h_6(\tilde{N}_f/2) g^2 c^2 \left( \frac{\tilde{N}_f^2}{32\pi^2 h_6(\tilde{N}_f/2)} + \frac{g^2}{c^3} \right), \quad (79)$$

$$\partial_\ell \chi_1 = z_\tau \chi_1 \left[ \left( \epsilon - \frac{g^2}{4\pi \tilde{N}_f} + \frac{32}{\tilde{N}_f^3} \frac{g^4}{c^2} h_6(\tilde{N}_f/2) \right) - \frac{9}{2\pi^2} \chi_1 \right]. \quad (80)$$

The analysis of the beta functions is rather involved, and the details are in Appendix B. Key elements of the final result are summarized in Fig. 15. In three dimensions, the system flows to a weakly coupled quasilocal marginal Fermi liquid if the initial Yukawa coupling is smaller than the boson velocity (below the dashed separatrix in Fig. 15a). On the other hand, the system flows to strong coupling regime as the boson velocity is renormalized to zero when initial Yukawa coupling is large (above the dashed separatrix in Fig. 15a). Below three dimensions, the boson velocity always flows to zero within a finite RG time (Fig. 15b), and the theory becomes non-perturbative.

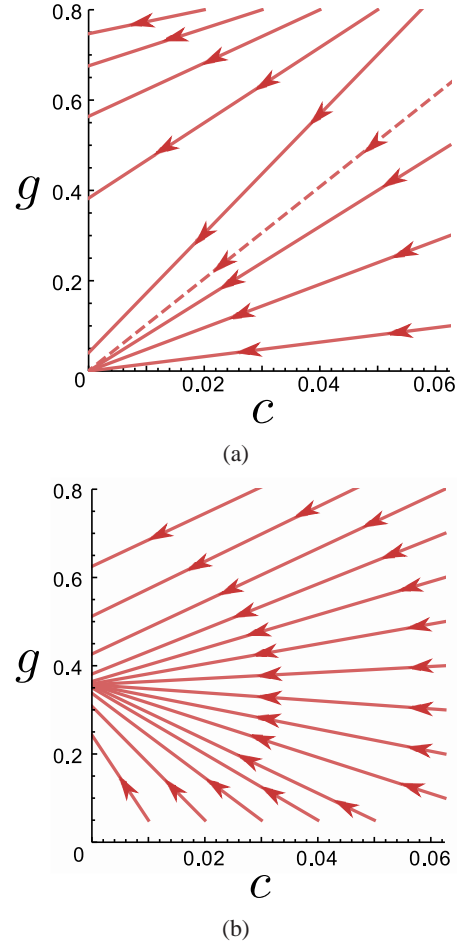


FIG. 15: RG flow of  $g$  and  $c$  at the CDW critical point with  $\tilde{N} = 2$  and  $v = v_* = 1$ . (a) In  $d = 3$  there is a fixed point at the origin with a finite basin of attraction; for flows originating outside the basin,  $c$  flows to zero after a finite RG time. The dashed line in (a) denotes the separatrix which divides the flows to the stable quasilocal marginal Fermi liquid (below the separatrix) from the flow toward the non-perturbative regime (above the separatrix). (b) In  $d = 3 - \epsilon$ ,  $c$  flows to zero after a finite RG time with a finite  $g$ . For the plot we have chosen  $\epsilon = 0.01$ .

When the system flows to the strong coupling regime, there are several possibilities. First, the system may still flow to a strongly interacting non-Fermi liquid fixed point. Second,  $c^2$  may become negative at low energies, which results in a shift of the ordering vector, possibly towards an incommensurate CDW ordering [66]. In this case, the commensurate CDW can not occur without further fine tuning. Third, the system may develop an instability toward other competing order, such as superconductivity [67]. Finally, a first order transition is a possibility.

The difference between the SDW and CDW critical points is summarized in Table III. The differences arise from the fact that the vertex correction screens (anti-screens) the interaction for the CDW (SDW) critical point. Within the present

	SDW	CDW
$d = 3$	Quasiloca MFL	<ul style="list-style-type: none"> <li>• Non-perturbative (<math>g_0^2 &gt; c_0^2</math>)</li> <li>• Quasiloca MFL (<math>g_0^2 &lt; c_0^2</math>)</li> </ul>
$d = 3 - \epsilon$	Anisotropic NFL	Non-perturbative

TABLE III: Fate of the SDW and CDW critical points in metals with  $C_2$  symmetry. Here NFL and MFL represents non-Fermi liquid and marginal Fermi liquid, respectively.

framework, it is also possible to consider a SDW critical point where the  $SU(N_c)$  spin rotational symmetry is explicitly broken down to a subgroup. In the Ising case where only one mode becomes critical at the critical point, the Yukawa vertex is commuting as in the CDW case. Therefore, we expect that the Ising SDW critical point will be similar to the CDW critical point. The easy-plane SDW criticality with  $N_c = 2$  [70] is special in that the one-loop Yukawa vertex correction vanishes due to  $\sum_{a=1}^2 \tau^a \tau^b \tau^a = 0$ . In this case, the two-loop diagram fails to prevent  $c$  from flowing to zero. Thus, one has to consider higher order self-energy and vertex corrections to determine the fate of the critical point.

## VI. SUMMARY AND DISCUSSION

In this work, we studied the spin and charge density wave critical point in metals with the  $C_2$  symmetry, where a one dimensional Fermi surface is embedded in space dimensions three and below. Within one-loop RG analysis augmented by a two-loop diagram, we obtained an anisotropic non-Fermi liquid below three dimensions at the SDW critical point. The Green's function near the hot spots and the spin-spin correlation function obey the anisotropic scaling, where not only frequency but also different components of momentum acquire non-trivial anomalous dimensions. Consequently, the Fermi surface develops an algebraic nesting near the hot spots with a universal shape. The stable non-Fermi liquid fixed point turns into a quasilocal marginal Fermi liquid in three dimensions, where the boson velocity along the ordering vector flows to zero compared to the Fermi velocity. In contrast to the SDW

criticality, the CDW critical point flows to a non-perturbative regime below three dimensions, while there is a finite parameter regime where the marginal Fermi liquid is still stable in three dimensions.

At the SDW critical point, it is expected that superconducting, pair density wave and charge density wave fluctuations are enhanced [26, 37, 68, 69]. At the one-loop order, the pattern of enhancement is expected to be similar to the case with the  $C_4$  symmetry. However, it will be of interest to examine the effects of anisotropic scaling through a comparative study. In particular, the stronger nesting in the  $C_2$  case will increase the phase space for the zero-energy particle-particle excitations with momentum  $2k_F$ . This will help enhance the pair density wave fluctuations, which was found to be as strong as the  $d$ -wave superconducting fluctuations at the one-loop order in the  $C_4$  case [37].

## VII. ACKNOWLEDGMENT

We thank Luis Balicas, Peter Lunts and Subir Sachdev for helpful discussions, and Philipp Strack for drawing our attention to several recent works. The research was supported in part by the Natural Sciences and Engineering Research Council of Canada (Canada) and the Early Research Award from the Ontario Ministry of Research and Innovation. Research at the Perimeter Institute is supported in part by the Government of Canada (Canada) through Industry Canada, and by the Province of Ontario through the Ministry of Research and Information.

- 
- |   |  |
|---|--|
| <p>[1] G. R. Stewart, Rev. Mod. Phys. <b>73</b>, 797 (2001).<br/> [2] H. v. Löhneysen, A. Rosch, M. Vojta, and P. Wölfle, Rev. Mod. Phys. <b>79</b>, 1015 (2007).<br/> [3] P. Gegenwart, Q. Si, and F. Steglich, Nature Physics <b>4</b>, 186 - 197 (2008).<br/> [4] N. P. Armitage, P. Fournier, and R. L. Greene, Rev. Mod. Phys. <b>82</b>, 2421 (2010).<br/> [5] T. Helm, M. V. Kartsovnik, I. Sheikin, M. Bartkowiak, F. Wolff-Fabris, N. Bittner, W. Biberacher, M. Lambacher, A. Erb, J. Wosnitzer, and R. Gross, Phys. Rev. Lett. <b>105</b>, 247002 (2010).<br/> [6] K. Hashimoto, K. Cho, T. Shibauchi, S. Kasahara, Y. Mizukami, R. Katsumata, Y. Tsuruhara, T. Terashima, H. Ikeda,</p> | <p>M. A. Tanatar, H. Kitano, N. Salovich, R. W. Giannetta, P. Walmsley, A. Carrington, R. Prozorov, and Y. Matsuda, Science <b>336</b>, 1554 (2012).<br/> [7] T. Park, F. Ronning, H. Yuan, M. Salamon, R. Movshovich, J. Sarrao, and J. Thompson, Nature (London) <b>440</b>, 65 (2006).<br/> [8] T. Moriya and J. Kawabata, J. Phys. Soc. Jpn. <b>34</b>, 639 (1973).<br/> [9] T. Moriya and J. Kawabata, J. Phys. Soc. Jpn. <b>35</b>, 669 (1973).<br/> [10] J. A. Hertz, Phys. Rev. B <b>14</b>, 1165 (1976).<br/> [11] A. J. Millis, Phys. Rev. B <b>48</b>, 7183 (1993).<br/> [12] T. Holstein, R. E. Norton, and P. Pincus, Phys. Rev. B <b>8</b>, 2649 (1973).<br/> [13] M. Y. Reizer, Phys. Rev. B <b>40</b>, 11571 (1989).</p> |
|---|--|



- [14] P. A. Lee, Phys. Rev. Lett. **63**, 680 (1989).
- [15] P. A. Lee and N. Nagaosa, Phys. Rev. B **46**, 5621 (1992).
- [16] B. L. Altshuler, L. B. Ioffe, and A. J. Millis, Phys. Rev. B **50**, 14048 (1994).
- [17] J. Polchinski, Nucl. Phys. B **422**, 617 (1994).
- [18] Y. B. Kim, A. Furusaki, X.-G. Wen, and P. A. Lee, Phys. Rev. B **50**, 17917 (1994).
- [19] B. I. Halperin, P. A. Lee, and N. Read, Phys. Rev. B **47**, 7312 (1993).
- [20] A. V. Chubukov, Europhys. Lett. **44**, 655 (1998).
- [21] Ar. Abanov and A. V. Chubukov, Phys. Rev. Lett. **84**, 5608 (2000).
- [22] Ar. Abanov, A. V. Chubukov, and J. Schmalian, Adv. in Phys. **52**, 119 - 218 (2003).
- [23] S. Sur & S.-S. Lee, Phys. Rev. B **90**, 045121 (2014).
- [24] S.-S. Lee, Phys. Rev. B **80**, 165102 (2009).
- [25] M. A. Metlitski and S. Sachdev, Phys. Rev. B **82**, 075127 (2010).
- [26] M. A. Metlitski and S. Sachdev, Phys. Rev. B **82**, 075128 (2010).
- [27] T. Holder and W. Metzner, Phys. Rev. B **92**, 041112(R) (2015)
- [28] S. Chakravarty, R. E. Norton, and O. F. Syljuåsen, Phys. Rev. Lett., **74**, 1423 (1995).
- [29] A. L. Fitzpatrick, S. Kachru, J. Kaplan, and S. Raghu, Phys. Rev. B **88**, 125116 (2013).
- [30] A. L. Fitzpatrick, S. Kachru, J. Kaplan, and S. Raghu, Phys. Rev. B **89**, 165114 (2014).
- [31] S.-S. Lee, Phys. Rev. B **78**, 085129 (2008).
- [32] I. Mandal and S.-S. Lee, Phys. Rev. B **92** 035141, (2015).
- [33] C. Nayak and F. Wilczek, Nucl. Phys. B **417**, 359 (1994); Nucl. Phys. B **430**, 534 (1994).
- [34] D. F. Mross, J. McGreevy, H. Liu, and T. Senthil, Phys. Rev. B **82**, 045121 (2010).
- [35] T. Senthil and R. Shankar, Phys. Rev. Lett. **102**, 046406 (2009).
- [36] D. Dalidovich & S.-S. Lee, Phys. Rev. B **88**, 245106 (2013).
- [37] S. Sur & S.-S. Lee, Phys. Rev. B **91**, 125136 (2015).
- [38] A. A. Patel, P. Strack, and S. Sachdev, Phys. Rev. B **92**, 165105 (2015).
- [39] S. A. Maier and P. Strack, Phys. Rev. B **93**, 165114 (2016)
- [40] N. D.-Leyraud and L. Taillefer, Physica C **481**, 161 (2012).
- [41] J.-H. Chu, J. G. Analytis, C. Kucharczyk, and I. R. Fisher, Phys. Rev. B **79**, 014506 (2009).
- [42] T.-M. Chuang, M. P. Allan, Jinho Lee, Yang Xie, Ni Ni, S. L. Budko, G. S. Boebinger, P. C. Canfield, and J. C. Davis, Science **327**, 181 (2010).
- [43] M. J. Lawler, K. Fujita, Jinhwan Lee, A. R. Schmidt, Y. Kohsaka, Chung Koo Kim, H. Eisaki, S. Uchida, J. C. Davis, J. P. Sethna, and Eun-Ah Kim, Nature **466**, 347 (2010).
- [44] Y. Ando, K. Segawa, S. Komiyama, and A. N. Lavrov, Phys. Rev. Lett. **88**, 137005 (2002).
- [45] J. Fink, V. Soltwisch, J. Geck, E. Schierle, E. Weschke, and B. Büchner, Phys. Rev. B **83**, 092503 (2011).
- [46] V. Hinkov, D. Haug, B. Fauqu, P. Bourges, Y. Sidis, A. Ivanov, C. Bernhard, C. T. Lin, B. Keimer, Science **319**, 597 (2008).
- [47] S. A. Kivelson, E. Fradkin, and V. J. Emery, Nature **393**, 550 (1998).
- [48] A. V. Chubukov, Springer Series in Materials Science, Volume 211, 2015, pp 255-329.
- [49] J.-H. Chu, J. G. Analytis, K. De Greve, P. L. McMahon, Z. Islam, Y. Yamamoto, and I. R. Fisher, Science **329**, 824 (2010).
- [50] S. Kasahara, H. J. Shi, K. Hashimoto, S. Tonegawa, Y. Mizukami, T. Shibauchi, K. Sugimoto, T. Fukuda, T. Terashima, A. H. Nevidomskyy, and Y. Matsuda, Nature **486**, 382 (2012).
- [51] R. Zhou, Z. Li, J. Yang, D.L. Sun, C. T. Lin and G.-Q. Zheng, Nature Comm. **4**, 2265 (2013).
- [52] X. Lu, J. T. Park, R. Zhang, H. Luo, A. H. Nevidomskyy, Q. Si, P. Dai, Science **345**, 657(2014).
- [53] E. Thewalt, J. P. Hinton, I. Hayes, T. Helm, D. H. Lee, James G. Analytis, and J. Orenstein, arXiv:1507.03981.
- [54] T. Holder and W. Metzner, Phys. Rev. B **90**, 161106(R) (2014).
- [55] T. Schäfer, A. A. Katanin, K. Held, and A. Toschi, arXiv:1605.06355
- [56] C. Nayak, Phys. Rev. B **62**, 4880 (2000).
- [57] A. A. Burkov, M. D. Hook, and Leon Balents, Phys. Rev. B **84**, 235126 (2011).
- [58] G. Bian, T.-R. Chang, R. Sankar, S.-Y. Xu, H. Zheng, T. Neupert, C.-K. Chiu, S.-M. Huang, G. Chang, I. Belopolski, D. S. Sanchez, M. Neupane, N. Alidoust, C. Liu, B. Wang, C.-C. Lee, H.-T. Jeng, C. Zhang, Z. Yuan, S. Jia, A. Bansil, F. Chou, H. Lin, and M. Z. Hasan, Nature Communications **7**, 10556 (2016).
- [59] According to Eq. (49), we have  $J_{l,0,n}^{(\lambda)}(v, \epsilon) = 0$  for  $\lambda = v, c, g$ , and  $J_{l,m,n < 2}^{(\lambda)}(v, \epsilon) = 0$  for  $\lambda = v, g$ . Because  $v$  can be renormalized only in the presence of  $g$ , one also has  $J_{0,m,n}^{(v)}(v, \epsilon) = 0$ . Furthermore, the full  $(d + 1)$ -dimensional rotational invariance in the bosonic sub-sector implies  $J_{0,m,n}^{(c)}(v, \epsilon) = 0$ .
- [60] M. Nakajima, T. Lianga, S. Ishida, Y. Tomioka, K. Kihou, C. H. Leeb, A. Iyob, H. Eisakib, T. Kakeshita, T. Itob, and S. Uchida, PNAS **108**, 12238 (2011).
- [61] A. Dusz, A. Lucarelli, F. Pfuner, J.-H. Chu, I. R. Fisher, and L. Degiorgi, Europhys. Lett. **93**, 37002 (2011).
- [62] M. A. Tanatar, E. C. Blomberg, A. Kreyssig, M. G. Kim, N. Ni, A. Thaler, S. L. Budko, P. C. Canfield, A. I. Goldman, I. I. Mazin, and R. Prozorov, Phys. Rev. B **81**, 184508 (2010).
- [63] B. Valenzuela, E. Bascones, and M. J. Calderin, Phys. Rev. Lett. **105**, 207202 (2010).
- [64] J. Rech, C. Pépin, and A. V. Chubukov, Phys. Rev. B **74**, 195126 (2006).
- [65] C. M. Varma, P. B. Littlewood, S. Schmitt-Rink, E. Abrahams, and A. E. Ruckenstein, Phys. Rev. Lett. **63**, 1996 (1989).
- [66] C. Castellani, C. Di Castro, and M. Grilli, Z. Phys. B Con. Mat. **103**, 137 (1996).
- [67] Y. Wang and A. V. Chubukov, arXiv:1507.03583.
- [68] E. Berg, M. A. Metlitski and S. Sachdev, Science **338**, 1606 (2012).
- [69] Y. Schattner, M. H. Gerlach, S. Trebst, E. Berg, arXiv:1512.07257
- [70] C. M. Varma, Phys. Rev. Lett. **115**, 186405 (2015).



## Appendix A: Computation of Feynman diagrams

In this appendix we show the key steps for computing the Feynman diagrams.

### 1. One loop diagrams

#### a. Electron self energy

The quantum correction to the electron self-energy from the diagram in Fig. 3a is

$$\delta S^{(2,0)} = \mu^{3-d} 2\mathcal{B}_{(2,0)}^{(1L)} g^2 \sum_{n=\pm} \sum_{s=1}^{N_c} \sum_{j=1}^{N_f} \int dk \bar{\Psi}_{n,s,j}(k) \Upsilon_{(2,0)}^{(n)}(k) \Psi_{n,s,j}(k), \quad (\text{A1})$$

where

$$\mathcal{B}_{(2,0)}^{(1L)} = \begin{cases} \frac{N_c^2 - 1}{N_f N_c} & \text{for SDW} \\ \frac{1}{N_f N_c} & \text{for CDW} \end{cases} \quad (\text{A2})$$

and

$$\Upsilon_{(2,0)}^{(n)}(k) = \int \frac{d^{d-1}\mathbf{Q}}{(2\pi)^{d-1}} \frac{d^2\vec{q}}{(2\pi)^2} \gamma_{d-1} G_{\bar{n}}(k+q) \gamma_{d-1} D(q). \quad (\text{A3})$$

The bare Green's functions are given by

$$G_n(k) = -i \frac{\mathbf{\Gamma} \cdot \mathbf{K} + \gamma_{d-1} \varepsilon_n(\vec{k})}{|\mathbf{K}|^2 + \varepsilon_n^2(\vec{k})}, \quad (\text{A4})$$

$$D(q) = \frac{1}{|\mathbf{Q}|^2 + q_x^2 + c^2 q_y^2}. \quad (\text{A5})$$

After the integrations over  $\vec{q}$  and  $\mathbf{Q}$ , Eq. (A3) can be expressed in terms of a Feynman parameter,

$$\begin{aligned} \Upsilon_{(2,0)}^{(n)}(k) &= \frac{i}{(4\pi)^{(d+1)/2}} \Gamma\left(\frac{3-d}{2}\right) \int_0^1 dx \sqrt{\frac{1-x}{c^2 + x(1-(1-v^2)c^2)}} \\ &\times \left[ x(1-x) \left\{ |\mathbf{K}|^2 + \frac{c^2 \varepsilon_{\bar{n}}^2(\vec{k})}{c^2 + x(1-(1-v^2)c^2)} \right\} \right]^{-\frac{3-d}{2}} \left[ \mathbf{K} \cdot \mathbf{\Gamma} - \frac{c^2 \varepsilon_{\bar{n}}(\vec{k}) \gamma_{d-1}}{c^2 + x(1-(1-v^2)c^2)} \right]. \end{aligned} \quad (\text{A6})$$

The UV divergent part in the  $d \rightarrow 3$  limit is given by

$$\Upsilon_{(2,0)}^{(n)}(k) = \frac{i}{8\pi^2 \epsilon} \left[ h_1(v, c) \mathbf{K} \cdot \mathbf{\Gamma} - h_2(v, c) \varepsilon_{\bar{n}}(\vec{k}) \gamma_{d-1} \right], \quad (\text{A7})$$

where

$$h_1(v, c) = \int_0^1 dx \sqrt{\frac{1-x}{c^2 + x(1-(1-v^2)c^2)}}, \quad h_2(v, c) = c^2 \int_0^1 dx \sqrt{\frac{1-x}{[c^2 + x(1-(1-v^2)c^2)]^3}}. \quad (\text{A8})$$

This leads to the one-loop counter term for the electron self-energy,

$$S_{CT}^{(2,0)} = -\frac{\mathcal{B}_{(2,0)}^{(1L)}}{4\pi^2 \epsilon} g^2 \sum_{n=\pm} \sum_{s=1}^{N_c} \sum_{j=1}^{N_f} \int dk$$

$$\times \bar{\Psi}_{n,s,j}(k) \left[ i h_1(v, c) \mathbf{K} \cdot \mathbf{\Gamma} - i h_2(v, c) \varepsilon_{\bar{n}}(\vec{k}) \gamma_{d-1} \right] \Psi_{n,s,j}(k). \quad (\text{A9})$$

*b. Boson self energy*

The boson self energy in Fig. 3b is given by

$$\delta S^{(0,2)} = -\mu^{3-d} \frac{g^2}{2} \int dq \Upsilon_{(0,2)}(q) \text{Tr}(\Phi(-q)\Phi(q)), \quad (\text{A10})$$

where

$$\Upsilon_{(0,2)}(q) = \sum_{n=\pm} \int dk \text{Tr}[\gamma_{d-1} G_n(k+q) \gamma_{d-1} G_{\bar{n}}(k)]. \quad (\text{A11})$$

We first integrate over  $\vec{k}$ . Because  $\vec{q}$  can be absorbed into the internal momentum  $\vec{k}$ ,  $\Upsilon_{(0,2)}(q)$  is independent of  $\vec{q}$ . Using the Feynman parameterization, we write the resulting expression as

$$\Upsilon_{(0,2)}(q) = \frac{1}{2\pi v} \int_0^1 dx \int \frac{d^{d-1}\mathbf{K}}{(2\pi)^{d-1}} \frac{[x(1-x)]^{-\frac{1}{2}} \mathbf{K} \cdot (\mathbf{K} + \mathbf{Q})}{x|\mathbf{K} + \mathbf{Q}|^2 + (1-x)|\mathbf{K}|^2}. \quad (\text{A12})$$

The quadratically divergent term is the mass renormalization, which is automatically tuned away at the critical point in the present scheme. The remaining correction to the kinetic energy of the boson becomes

$$\Upsilon_{(0,2)}(q) = -\frac{|\mathbf{Q}|^2}{16\pi v \epsilon} \quad (\text{A13})$$

up to finite terms. Accordingly we add the following counter term,

$$S_{CT}^{(0,2)} = -\frac{1}{4} \frac{1}{8\pi \epsilon} \frac{g^2}{v} \int dq |\mathbf{Q}|^2 \text{Tr}(\Phi(-q)\Phi(q)). \quad (\text{A14})$$

*c. Yukawa vertex correction*

The diagram in Fig. 3c gives rise to the vertex correction in the quantum effective action,

$$\begin{aligned} \delta S^{(2,1)} &= i \frac{g}{\sqrt{N_f}} \mu^{\frac{3(3-d)}{2}} 2\mathcal{B}_{(2,1)}^{(1L)} g^2 \sum_{j=1}^{N_f} \sum_{s,s'=1}^{N_c} \\ &\times \int dk dq \left[ \bar{\Psi}_{+,j,s}(k+q) \Upsilon_{(2,1)}^{(+,-)}(k, q) \Phi_{s,s'}(q) \Psi_{-,j,s'}(k) - \text{h.c.} \right], \end{aligned} \quad (\text{A15})$$

where

$$\Upsilon_{(2,1)}^{(n,\bar{n})}(k, q) = \int dp \gamma_{d-1} G_{\bar{n}}(p+q+k) \gamma_{d-1} G_n(p+k) \gamma_{d-1} D(p) \quad (\text{A16})$$

and

$$\mathcal{B}_{(2,1)}^{(1L)} = \begin{cases} \frac{1}{N_c N_f} & \text{for SDW} \\ -\frac{1}{N_c N_f} & \text{for CDW} \end{cases}. \quad (\text{A17})$$

The minus sign in  $\mathcal{B}_{(2,1)}^{(1L)}$  for the SDW case is due to the anti-commuting nature of the  $SU(N_c)$  generators,  $\sum_{a=1}^{N_c^2-1} \tau^a \tau^b \tau^a = -\frac{2}{N_c} \tau^b$ . The UV divergent part in the  $\epsilon \rightarrow 0$  limit can be extracted by setting all external frequency and momenta to zero

except  $\mathbf{Q}$ ,

$$\Upsilon_{(2,1)}^{(n,\bar{n})}(\mathbf{Q}) = \gamma_{d-1} \int dp \frac{|\mathbf{P}|^2 - \varepsilon_{\bar{n}}(\vec{p})\varepsilon_n(\vec{p})}{\left[|\mathbf{P}|^2 + p_x^2 + c^2 p_y^2\right] \left[|\mathbf{Q} + \mathbf{P}|^2 + \varepsilon_{\bar{n}}^2(\vec{p})\right] \left[|\mathbf{P}|^2 + \varepsilon_n^2(\vec{p})\right]}. \quad (\text{A18})$$

Eq. (A18) is evaluated following the computation in Ref. [37] to obtain

$$\Upsilon_{(2,1)}^{(n,\bar{n})}(\mathbf{K}) = \frac{\gamma_{d-1} v}{16\pi^3 \epsilon} h_3(v, c) + \mathcal{O}(\epsilon^0), \quad (\text{A19})$$

where

$$h_3(v, c) = \int_0^{2\pi} d\theta \int_0^1 dx_1 \int_0^{1-x_1} dx_2 \left[ \frac{1}{\zeta(\theta, x_1, x_2, v, c)} - \frac{v^2 \sin(2\theta)}{\zeta^2(\theta, x_1, x_2, v, c)} \right], \quad (\text{A20})$$

with

$$\begin{aligned} \zeta(\theta, x_1, x_2, v, c) &= 2v^2[x_1 \sin^2(\theta) + x_2 \cos^2(\theta)] \\ &\quad + (1 - x_1 - x_2) \left[ \sin^2\left(\theta + \frac{\pi}{4}\right) + c^2 v^2 \cos^2\left(\theta + \frac{\pi}{4}\right) \right]. \end{aligned} \quad (\text{A21})$$

Note that the UV divergent part of  $\Upsilon_{(2,1)}^{(n,\bar{n})}$  is independent of  $(n, \bar{n})$ . From this, we identify the counter term for the Yukawa vertex,

$$\begin{aligned} S_{CT}^{(2,1)} &= -i \frac{g}{\sqrt{N_f}} \frac{\mathcal{B}_{(2,1)}^{(1L)}}{8\pi^3 \epsilon} g^2 v h_3(v, c) \sum_{j=1}^{N_f} \sum_{s,s'=1}^{N_c} \\ &\quad \times \int dk dq \left[ \bar{\Psi}_{+,j,s}(k+q) \gamma_{d-1} \Phi_{s,s'}(q) \Psi_{-,j,s'}(k) - \text{h.c.} \right]. \end{aligned} \quad (\text{A22})$$

#### *d. $\phi^4$ vertex corrections*

There are two types of one-loop diagrams that can potentially contribute to the renormalization of the quartic vertex as is shown in Fig. 3d and Fig. 3e. The diagram in Fig. 3e is UV finite at  $d = 3$  [37], which implies that it does not contain an  $\epsilon^{-1}$  pole in  $d = 3 - \epsilon$ . The second type of diagrams are produced by the boson vertices only. They lead to non-zero counter terms,

$$\begin{aligned} S_{CT}^{(0,4)} &= \frac{1}{8\pi^2 c \epsilon} \int dq_1 dq_2 dq_3 \\ &\quad \times \left\{ \left[ \mathcal{B}_{(0,4)}^{(1L;1a)} u_1^2 + \mathcal{B}_{(0,4)}^{(1L;1b)} u_1 u_2 + \mathcal{B}_{(0,4)}^{(1L;1c)} u_2^2 \right] \text{Tr}(\Phi(-q_1 + q_2) \Phi(q_1)) \text{Tr}(\Phi(-q_3 - q_2) \Phi(q_3)) \right. \\ &\quad \left. + \left[ \mathcal{B}_{(0,4)}^{(1L;2a)} u_1 u_2 + \mathcal{B}_{(0,4)}^{(1L;2b)} u_2^2 \right] \text{Tr}(\Phi(-q_1 + q_2) \Phi(q_1) \Phi(-q_3 - q_2) \Phi(q_3)) \right\}. \end{aligned} \quad (\text{A23})$$

Here

$$\begin{aligned} \mathcal{B}_{(0,4)}^{(1L;1a)} &= N_c^2 + 7, \quad \mathcal{B}_{(0,4)}^{(1L;1b)} = \frac{2(2N_c^2 - 3)}{N_c}, \quad \mathcal{B}_{(0,4)}^{(1L;1c)} = \frac{3(N_c^2 + 3)}{N_c^2}, \\ \mathcal{B}_{(0,4)}^{(1L;2a)} &= 12, \quad \mathcal{B}_{(0,4)}^{(1L;2b)} = \frac{2(N_c^2 - 9)}{N_c} \end{aligned} \quad (\text{A24})$$

for the SDW case. For the CDW case, one can set  $u_2 = 0$  and  $\mathcal{B}_{(0,4)}^{(1L;1a)} = 9$ .

## 2. Two loops boson self-energy

There are five diagrams, shown in Fig. 10, that contribute to the boson self energy at the two-loop order. We will first show that only Fig. 10a contributes to the renormalization of  $c$  to the leading order in  $c$ . We will also outline the key steps for an explicit computation of Fig. 10a.

Let us denote the loop integrations in figures 10b - 10d for fixed electron flavor  $n$  as  $\Upsilon_{(0,2)}^{2L;b}(q)$ ,  $\Upsilon_{(0,2)}^{2L;c}(q)$  and  $\Upsilon_{(0,2)}^{2L;d}(q)$ , respectively, with  $q$  being the external frequency-momentum. At  $c = 0$  the loop integrations in Fig. 10b is given by

$$\Upsilon_{(0,2)}^{2L;b}(q) = \int \frac{d^4 p}{(2\pi)^4} \frac{d^4 k}{(2\pi)^4} \frac{\text{Tr}(\gamma_{d-1} G_{\bar{n}}(k) \gamma_{d-1} G_n(k+p) \gamma_{d-1} G_{\bar{n}}(k) \gamma_{d-1} G_n(k+q))}{|\mathbf{P}|^2 + p_x^2}. \quad (\text{A25})$$

The integrand depends on  $p_y$  only through

$$G_n(k+p) = [i(\mathbf{K} + \mathbf{P}) \cdot \mathbf{\Gamma} + (\varepsilon_n(k) + vp_x + np_y) \gamma_{d-1}]^{-1}. \quad (\text{A26})$$

Changing coordinate as  $p_y \mapsto p_y - n((\varepsilon_n(k) + vp_x))$ ,  $G_n(k+p)$  becomes independent of  $\vec{k}$ . Since  $\varepsilon_n(\vec{k})$  and  $\varepsilon_{\bar{n}}(\vec{k})$  are linearly independent, we can change coordinates as  $(k_x, k_y) \mapsto (\varepsilon_n(\vec{k}), \varepsilon_{\bar{n}}(\vec{k}))$  and shift  $\varepsilon_n(\vec{k}) \mapsto \varepsilon_n(\vec{k}) - \varepsilon_n(\vec{q})$  to make  $\Upsilon_{(0,2)}^{2L;b}(q)$  independent of  $\vec{q}$ . This shows that Fig. 10b does not depend on  $\vec{q}$  in the small  $c$  limit. Note that such dependence may arise at order  $g^4 c$  or higher, but these contributions are sub-dominant to that of Fig. 10a.

$\Upsilon_{(0,2)}^{2L;c}(q)$  and  $\Upsilon_{(0,2)}^{2L;d}(q)$  closely resemble  $\Upsilon_{(0,2)}(q)$ . Because the one-loop counter terms are independent of the  $x$  and  $y$  components of momentum, it is straightforward to shift the internal integration variable to show that  $\Upsilon_{(0,2)}^{2L;c}(q)$  and  $\Upsilon_{(0,2)}^{2L;d}(q)$  are independent of  $\vec{q}$ , irrespective of the value of  $c$ . Therefore, diagrams in Figs. 10c and 10d do not contribute to  $Z_{5,1}$  and  $Z_{6,1}$ . 10e is also sub-leading because  $\chi_i = 0$  at the one-loop fixed point.

The quantum correction due to Fig. 10a is

$$\delta S_{(0,2)}^{2L;a} = \mu^{2(3-d)} \frac{8\mathcal{B}_{(0,2)}^{(2L)}}{4} g^4 \int dq \Upsilon_{(0,2)}^{2L;a}(q) \text{Tr}(\Phi(-q)\Phi(q)) \quad (\text{A27})$$

where

$$\Upsilon_{(0,2)}^{2L;a}(q) = - \int dp dk \frac{\text{Tr}(\gamma_{d-1} G_+(k+q) \gamma_{d-1} G_-(p+q) \gamma_{d-1} G_+(p) \gamma_{d-1} G_-(k))}{|\mathbf{P} - \mathbf{K}|^2 + (p_x - k_x)^2 + c^2(p_y - k_y)^2} \quad (\text{A28})$$

and  $\mathcal{B}_{(0,2)}^{(2L)} = \mathcal{B}_{(2,1)}^{(1L)}$  as defined in Eq. (A17). In order to extract the leading order term that depends on  $\vec{k}$  in the small  $c$  limit, we set  $c = 0$  and  $\mathbf{Q} = 0$  in  $\Upsilon_{(0,2)}^{2L;a}(q)$  to write

$$\Upsilon_{(0,2)}^{2L;a}(\vec{q}) = - \int dp dk \frac{\text{Tr}(\gamma_{d-1} G_+(\mathbf{K}, \vec{k} + \vec{q}) \gamma_{d-1} G_-(\mathbf{P}, \vec{p} + \vec{q}) \gamma_{d-1} G_+(p) \gamma_{d-1} G_-(k))}{|\mathbf{P} - \mathbf{K}|^2 + (p_x - k_x)^2}. \quad (\text{A29})$$

Using  $\text{Tr}(\gamma_\mu \gamma_\nu) = 2\delta_{\mu,\nu} \mathcal{I}_2$ , we evaluate the trace in the numerator to obtain

$$\begin{aligned} \Upsilon_{(0,2)}^{2L;a}(\vec{q}) &= -2 \int dp dk \\ &\times \frac{[|\mathbf{K}|^2 - \varepsilon_+(\vec{k} + \vec{q}) \varepsilon_-(\vec{k})][|\mathbf{P}|^2 - \varepsilon_-(\vec{p} + \vec{q}) \varepsilon_+(\vec{p})] - \mathbf{K} \cdot \mathbf{P} [\varepsilon_+(\vec{k} + \vec{q}) + \varepsilon_-(\vec{k})][\varepsilon_-(\vec{p} + \vec{q}) + \varepsilon_+(\vec{p})]}{[|\mathbf{K}|^2 + \varepsilon_+^2(\vec{k} + \vec{q})][|\mathbf{K}|^2 + \varepsilon_-^2(\vec{k})][|\mathbf{P}|^2 + \varepsilon_-^2(\vec{p} + \vec{q})][|\mathbf{P}|^2 + \varepsilon_+^2(\vec{p})][|\mathbf{P} - \mathbf{K}|^2 + (p_x - k_x)^2]}. \end{aligned} \quad (\text{A30})$$

We change coordinates for both  $\vec{p}$  and  $\vec{k}$  as  $(k_x, k_y) \mapsto (k_+, k_-)$  with  $k_\pm = \varepsilon_\pm(\vec{k})$ , and shift  $k_+ \mapsto k_+ - \varepsilon_+(\vec{q})$  and  $p_- \mapsto p_- - \varepsilon_-(\vec{q})$  to rewrite the expression as

$$\begin{aligned} \Upsilon_{(0,2)}^{2L;a}(\vec{q}) &= -\frac{1}{2v^2} \int dp' dk' \\ &\times \frac{[|\mathbf{K}|^2 - k_+ k_-][|\mathbf{P}|^2 - p_+ p_-] - \mathbf{K} \cdot \mathbf{P} [k_+ + k_-][p_+ + p_-]}{[|\mathbf{K}|^2 + k_+^2][|\mathbf{K}|^2 + k_-^2][|\mathbf{P}|^2 + p_-^2][|\mathbf{P}|^2 + p_+^2][|\mathbf{P} - \mathbf{K}|^2 + \frac{1}{4v^2}(p_+ + p_- - k_+ - k_- + 2q_y)^2]}, \end{aligned} \quad (\text{A31})$$

where  $dk' \equiv \frac{d^{d-1}\mathbf{K}dk_+dk_-}{(2\pi)^{d+1}}$ . It is noted that  $\Upsilon_{(0,2)}^{2L;a}(\vec{q})$  has become *independent* of  $q_x$  in the small  $c$  limit. This implies that  $Z_{5,1}$  is at most order of  $g^4c$  which is negligible. From now on, we will focus on  $Z_{6,1}$ .

We integrate over  $\mathbf{P}$  and  $\mathbf{K}$  after introducing Feynman parameters,  $x, y$  and  $u, w$ . Employing a Schwinger parameter,  $\alpha$ , we have

$$\begin{aligned} \Upsilon_{(0,2)}^{2L;a}(\vec{q}) = & -\frac{1}{2\pi^2(4\pi)^{d+1}v^2} \int_0^1 dx du \int_0^{1-x} dy \int_0^{1-u} dw \frac{(1-u-w)^{(3-d)/2}}{A^{(d-1)/2}} \int_0^\infty d\alpha e^{-\alpha M^2} \\ & \times \int_{-\infty}^\infty dp_+ dp_- dk_+ dk_- \left[ \left\{ \frac{(d-1)^2}{4A} + \frac{d^2-1}{4A^2} (1-u-w)(1-x-y)^2 \right\} \alpha^{3-d} \right. \\ & - \frac{(d-1)(1-u-w)}{2A} \left\{ p_+ p_- + \left( (1-x-y)^2 + \frac{A}{1-u-w} \right) k_+ k_- \right. \\ & \left. \left. + (1-x-y)(k_+ + k_-)(p_+ + p_-) \right\} \alpha^{4-d} + (1-u-w) p_+ p_- k_+ k_- \alpha^{5-d} \right], \end{aligned} \quad (\text{A32})$$

where

$$\begin{aligned} A \equiv A(x, y, u, w) = & (u+w) + (x+y)(1-x-y)(1-u-w), \quad \text{and} \\ M^2 \equiv M^2(k_\pm, p_\pm; x, y, u, w; v, q_y) = & uk_+^2 + wk_-^2 + x(1-u-w)p_+^2 + y(1-u-w)p_-^2 \\ & + \frac{(1-u-w)(1-x-y)}{4v^2} (p_+ + p_- - k_+ - k_- + 2q_y)^2. \end{aligned} \quad (\text{A33})$$

At this stage, we subtract the mass renormalization from  $\Upsilon_{(0,2)}^{2L;a}(\vec{q})$  and proceed with the computation of  $\Delta\Upsilon_{(0,2)}^{2L;a}(\vec{q}) = \Upsilon_{(0,2)}^{2L;a}(\vec{q}) - \Upsilon_{(0,2)}^{2L;a}(0)$ . After integrating over  $p_\pm, k_\pm$  and  $\alpha$ , we extract the pole in  $\epsilon$  as

$$\Delta\Upsilon_{(0,2)}^{2L;a}(\vec{q}) = \frac{q_y^2 h_6(v)}{\epsilon v^2}. \quad (\text{A34})$$

Here the function  $h_6(v)$  is defined as

$$\begin{aligned} h_6(v) = & \frac{2}{(4\pi)^4} \int_0^1 dx du \int_0^{1-x} dy \int_0^{1-u} dw \frac{1}{A} \left[ \left\{ 1 + \frac{2}{A} (1-u-w)(1-x-y)^2 \right\} \frac{J_1}{A} \right. \\ & \left. - \left\{ 1 + \frac{1}{A} (1-u-w)(1-x-y)^2 \right\} J_2 - \frac{1-u-w}{A} \left\{ J_3 + (1-x-y)J_4 \right\} + (1-u-w)J_5 \right], \end{aligned} \quad (\text{A35})$$

where

$$\begin{aligned} J_1 \equiv J_1(\eta_i) = & \frac{\eta_5}{\sqrt{\eta_1\eta_2\eta_3\eta_4}}, \\ J_2 \equiv J_2(\eta_i, f_i) = & \frac{f_3}{\sqrt{\eta_1\eta_2\eta_3\eta_4}} \left[ \frac{\eta_5}{2\eta_4} - f_4(1+f_4) \right], \\ J_3 \equiv J_3(\eta_i, f_i) = & \frac{f_1}{\sqrt{\eta_1\eta_2\eta_3\eta_4}} \left[ \frac{\eta_5}{2} \left\{ f_2(1-f_2) \left( \frac{1}{\eta_3} + \frac{(1+f_3)^2}{\eta_4} \right) - \frac{1}{\eta_2} \right\} \right. \\ & \left. - f_2(1-f_2)(1+f_3)^2(1+f_4)^2 \right], \\ J_4 \equiv J_4(\eta_i, f_i) = & \frac{f_1 + f_2(1-f_1)}{\sqrt{\eta_1\eta_2\eta_3\eta_4}} \left[ \frac{\eta_5}{2} \left( \frac{1}{\eta_3} + \frac{(1+f_3)^2}{\eta_4} \right) - (1+f_3)(1+f_4)(f_3 + f_4(1+f_3)) \right], \\ J_5 \equiv J_5(\eta_i, f_i) = & \frac{f_1}{2\sqrt{\eta_1\eta_2\eta_3\eta_4}} \left[ \frac{\eta_5}{2\eta_4} \left( \frac{3f_2f_3(1-f_2)(1+f_3)^2}{\eta_4} + \frac{f_2(1-f_2)(2+3f_3)}{\eta_3} - \frac{f_3}{\eta_2} \right) \right. \\ & \left. - (1+f_4) \left( \frac{3f_2f_3(1-f_2)(1+f_3)^2(1+2f_4)}{\eta_4} + \frac{f_2f_4(1-f_2)(2+3f_3)}{\eta_3} - \frac{f_3f_4}{\eta_2} \right) \right], \end{aligned} \quad (\text{A36})$$

with

$$\eta_1 \equiv \eta_1(a_1, F) = a_1 + F,$$

$$\begin{aligned}
\eta_2 &\equiv \eta_2(a_i, F) = \frac{a_2 F + a_1(a_2 + F)}{a_1 + F}, \\
\eta_3 &\equiv \eta_3(a_i, u, F) = \frac{a_2 u F + a_1(a_2(u + F) + u F)}{a_2 F + a_1(a_2 + F)}, \\
\eta_4 &\equiv \eta_4(a_i, u, w, F) = \frac{a_2 u w F + a_1(a_2(w(u + F) + u F) + u w F)}{a_2 u F + a_1(a_2(u + F) + u F)}, \\
\eta_5 &\equiv \eta_5(a_i, u, w, F) = \frac{a_1 a_2 u w F}{a_2 u w F + a_1(a_2(w(u + F) + u F) + u w F)},
\end{aligned} \tag{A37}$$

$$\begin{aligned}
f_1 &\equiv f_1(a_1, F) = \frac{F}{a_1 + F}, \\
f_2 &\equiv f_2(a_i, F) = \frac{a_1 F}{a_2 F + a_1(a_2 + F)}, \\
f_3 &\equiv f_3(a_i, u, F) = -\frac{a_1 a_2 F}{a_2 u F + a_1(a_2(u + F) + u F)}, \\
f_4 &\equiv f_4(a_i, u, w, F) = -\frac{a_1 a_2 u F}{a_2 u w F + a_1(a_2(u F + w(u + F)) + u w F)}.
\end{aligned} \tag{A38}$$

The functions  $a_i$  and  $F$  are defined as,

$$\begin{aligned}
a_1 &\equiv a_1(x, u, w) = x(1 - u - w), & a_2 &\equiv a_2(y, u, w) = y(1 - u - w), \\
F &\equiv F(x, y, u, w; v) = \frac{(1 - x - y)(1 - u - w)}{4v^2}.
\end{aligned} \tag{A39}$$

Therefore, the counter term to  $\vec{q}$  dependent part of the bosonic kinetic energy is given by

$$\begin{aligned}
S_{(0,2);CT}^{(2L)} &= -\delta S_{(0,2)}^{2L;a} \\
&= -\frac{\mathcal{B}_{(0,2)}^{(2L)}}{4\epsilon} \frac{8g^4 h_6(v)}{v^2} \int dq q_y^2 \text{Tr}(\Phi(-q)\Phi(q)),
\end{aligned} \tag{A40}$$

which gives

$$Z_{5,1} = 0, \tag{A41}$$

$$Z_{6,1} = -8\mathcal{B}_{(0,2)}^{(2L)} \frac{g^4 h_6(v)}{v^2 c^2} \tag{A42}$$

to the leading order in  $c$ .

## Appendix B: Analysis of RG flow at the CDW critical point

In this appendix, we provide an analysis of the RG flow predicted by the beta functions in Eqs. (78) - (80). Let us first analyze the flow in  $d = 3$  (Fig. 15a). According to Eq. (79),  $c(\ell)$  always decreases with increasing length scale. If the initial value of  $c$  is sufficiently small such that  $c_0 \ll \pi/(\tilde{N}_f + 2)$ , the inequality will be always satisfied at lower energies. In this case, one can ignore the last term in Eq. (78) to obtain a logarithmically decreasing Yukawa coupling,

$$g^2(\ell) = \frac{g_0^2}{1 + \alpha_g(\tilde{N}_f) g_0^2 \ell}, \tag{B1}$$

where  $g_0 \equiv g(\ell = 0)$  and  $\alpha_g(\tilde{N}_f) = \frac{1}{4\pi\tilde{N}_f} \left(1 + \frac{4}{\tilde{N}_f + 2}\right)$ .

The RG flow of  $c$  is relatively more complicated due to the important role of the two-loop correction. When  $g^2 \ll$



$\frac{c^3}{\pi^2 \tilde{N}_f \alpha_c(\tilde{N}_f)}$ , where  $\alpha_c(\tilde{N}_f) = \frac{32}{\tilde{N}_f^3} h_6(\tilde{N}_f/2)$ , the second term on the right hand side of Eq. (79) is negligible. In this case, the beta function for  $c$  gives

$$c(\ell) = c_0 \left[ 1 + \frac{c_0}{\pi^2 \tilde{N}_f \alpha_g(\tilde{N}_f)} \ln \left( 1 + \alpha_g(\tilde{N}_f) g_0^2 \ell \right) \right]^{-1}, \quad (\text{B2})$$

where we have utilized the expression for  $g(\ell)$  in Eq. (B1). Since  $g^2(\ell) \sim \ell^{-1}$  and  $c(\ell) \sim (\ln \ell)^{-1}$  in the  $\ell \rightarrow \infty$  limit, the second term on the right hand side of Eq. (79) becomes even smaller compared to the first term as  $\ell$  increases, which justifies Eq. (B2) at all  $\ell > 0$ . The quartic coupling flows to zero as  $\chi_1(\ell) \sim \ell^{-1}$ . Therefore, all the parameters, except for  $v$ , flow to zero in the low energy limit. Although  $c$  flows to zero, the critical point remains perturbatively controlled because  $g$  flows to zero much faster, such that  $g^2/c \ll 1$ . This is a stable quasilocal marginal Fermi liquid (MFL) [65].

In contrast, the first term on the right hand side of Eq. (79) is negligible if  $g^2 \gg \frac{c^3}{\pi^2 \tilde{N}_f \alpha_c(\tilde{N}_f)}$ , in which case we obtain

$$c(\ell) = \sqrt{\frac{c_0^2 - (2\alpha_c(\tilde{N}_f) g_0^2 - \alpha_g(\tilde{N}_f) c_0^2) g_0^2 \ell}{1 + \alpha_g(\tilde{N}_f) g_0^2 \ell}}. \quad (\text{B3})$$

We note that the coefficient of  $\ell$  in the numerator in Eq. (B3) depends on the initial values of  $g$  and  $c$ . If  $g_0^2 > \frac{\alpha_g(\tilde{N}_f) c_0^2}{2\alpha_c(\tilde{N}_f)}$ , which automatically implies  $g^2 \gg \frac{c^3}{\pi^2 \tilde{N}_f \alpha_c(\tilde{N}_f)}$  for small  $c$ , the boson velocity becomes zero at a *finite* RG time

$$\ell_0 = \frac{c_0^2/g_0^2}{2\alpha_c(\tilde{N}_f) g_0^2 - \alpha_g(\tilde{N}_f) c_0^2}. \quad (\text{B4})$$

This is different from the first case where  $c$  vanishes only asymptotically while the ratio  $g^2/c$  remains small. In the current case, the ratio  $g^2/c$  blows up, resulting in a loss of control over the perturbative expansion. For example, as  $\ell \rightarrow \ell_0$ ,  $\chi_1$  diverges as  $(\ell_0 - \ell)^{-a(c_0, g_0, \tilde{N}_f)}$  with  $a(c_0, g_0, \tilde{N}_f) = \min \left\{ 1, \frac{\alpha_c(\tilde{N}_f) g_0^4 \ell_0}{c_0^2 (1 + \alpha_g(\tilde{N}_f) g_0^2 \ell_0)} \right\}$ , which results in the theory becoming non-perturbative.

Finally, let us consider the case where  $\frac{c_0^3}{\pi^2 \tilde{N}_f \alpha_c(\tilde{N}_f)} \ll g_0^2 < \frac{\alpha_g(\tilde{N}_f) c_0^2}{2\alpha_c(\tilde{N}_f)}$ . In this case,  $c$  initially approaches a nonzero constant dictated by Eq. (B3). However, the system eventually enters into the regime with  $g^2 \ll \frac{c^3}{\pi^2 \tilde{N}_f \alpha_c(\tilde{N}_f)}$  at sufficiently large length scale. This is because  $g$  decreases much faster than  $c$  in this regime. Therefore the system again flows to the quasilocal marginal Fermi liquid.

Having understood the fate of the critical point in three dimensions, we consider the case below three dimensions (Fig. 15b). For  $\epsilon > 0$ ,  $g^2 \sim \epsilon$  as long as  $c$  is initially small. On the other hand,  $c$  flows to zero in a finite RG time. Consequently, the system becomes strongly coupled in the low energy limit.